Grain Size Variations Record Segregation of Residual Melts in Slow Spreading Oceanic Crust (Atlantis Bank, 57°E Southwest Indian Ridge)

C. Ferrando, L. France, V. Basch, A. Sanfilippo, R. Tribuzio, M. Boulanger

JGR Solid Earth

Key Points:
- Geochemical zoning in coarse crystals record crystallization of primitive crystal mush and subsequent reactive melt migration thereof
- Fine-grained olivine gabbros testify collection of residual melts from the crystal mush; their crystallization is dominated by nucleation
- Accumulation of migrating melts could have promoted extraction of those melts that potentially contribute to Mid Ocean Ridge Basalt erupted at the seafloor

Supporting Information:
- Supporting Information S1
- Table S2

Correspondence to:
C. Ferrando,
ottaferrando@gmail.com

Grain Size Variations Record Segregation of Residual Melts in Slow-Spreading Oceanic Crust (Atlantis Bank, 57°E Southwest Indian Ridge)

C. Ferrando[1,2] , L. France[1] , V. Basch[2] , A. Sanfilippo[2] , R. Tribuzio[2] , and M. Boulanger[1]

[1]Université de Lorraine, CNRS, CRPG, Nancy, France, [2]Dipartimento di Scienze della Terra e dell'Ambiente, Università degli Studi di Pavia, Pavia, Italy

Abstract Beneath slow-spreading ridges, melt bodies are generally considered to represent ephemeral magma reservoirs filled with crystal mushes. Formation of the oceanic crust requires at least partial extraction of melts from these crystal mushes. However, melts collection and extraction are processes yet to be fully constrained. We investigate olivine gabbros from the plutonic section recovered at the IODP Hole U1473A, in the Atlantis Bank Oceanic Core Complex (Southwest Indian Ridge), to unravel (i) the process of melt migration through lower crustal crystal mushes, and (ii) the collection and segregation of melts forming discrete microgabbro intervals. Throughout the Hole, fine- to coarse-grained intervals are widespread in olivine gabbros. Along the contacts, coarse-grained minerals display resorbed grain boundaries against the fine-grained minerals, suggesting partial dissolution by the melt crystallizing the fine-grained material. Coarse-grained plagioclase and clinopyroxene are zoned, showing progressive chemical evolution from more primitive crystal cores to more evolved crystal rims. Fine-grained minerals are unzoned and chemically similar to rims of coarse-grained minerals, indicating a genetic relationship. We attribute significant enrichments in the most incompatible elements of plagioclase and clinopyroxene to a magma evolution process associated with reactive melt migration. As temperature decreased, melts residual from the reactive processes were segregated in magma pockets that ultimately crystallize the fine-grained intervals (microgabbros). We document, for the first time, that these microgabbros are crystallization products of melts modified by reactive melt migration; the melts were extracted from the crystal mush and accumulated into discrete melt-rich zones. This process could have promoted partial extraction of those melts that in turn potentially contribute to Mid Ocean Ridge Basalts erupted at the seafloor.

1. Introduction

Beneath mid-ocean ridge axes, the lower crustal sections are believed to be composed predominantly of crystal mushes (e.g., Boulanger et al., 2020; Dick et al., 2008; Gillis et al., 2014; Lissenberg et al., 2019; Sinton & Detrick, 1992), apparently containing only few percent of interstitial melt. Although meter-thick melt-rich lenses are locally present under fast-spreading centers (e.g., Canales et al., 2009; J. S. Collier & Singh, 1998; Dunn et al., 2000; France et al., 2009), at slow- to ultraslow-spreading ridges such as at the Southwest Indian Ridge, magma lenses were imaged but no steady-state magma reservoirs are believed to persist over the duration of the opening of the ocean (e.g., Jian et al., 2017; Singh et al., 2006; Sinha et al., 1997). Rather, ephemeral magma bodies are considered to exist (e.g., Dick et al., 2003; Gracia et al., 1999; Tucholke et al., 1997). The crystal mush reservoirs are composed of a permeable crystal matrix with melt stored in the pore space, as more generally described for magma chambers at continental magmatic systems (Cashman et al., 2017).

Accretion of slow- to ultraslow-spreading lower oceanic crust is mainly accommodated by tectonic extension involving long-lived detachment faults and exhumation of gabbroic sequences on the seafloor at Oceanic Core Complexes (OCC; e.g., Blackman et al., 2011; Cannat et al., 2006; Escartín et al., 2008; MacLeod et al., 2009). These lower crustal sequences form through a complex history of multiple magmatic intrusions that are emplaced in an actively deforming environment. Magmatic differentiation, driven by fractional crystallization (e.g., Abily & Ceuleneer, 2013; Elthon, 1979; Grove et al., 1992; O'Neill & Jenner, 2012;

Ross & Elthon, 1997; Villiger et al., 2007) and in situ crystallization (e.g., Coogan & O'Hara, 2015; Langmuir, 1989; O'Hara & Fry, 1996), has been widely considered as one of the predominant processes responsible for the formation of the gabbroic crust. However, melt crystallization can be accompanied by additional magmatic processes that lead to further geochemical complexity during the magmatic evolution, namely (i) entrapment of melt portions, leading to the formation of chemically evolved crystal rims (e.g., Bédard, 1994; Bédard et al., 2009), and/or (ii) migration of buoyant and reactive melts through the crystal matrix. The migration of melts, either residual from the crystallization of primitive phases (e.g., Lissenberg et al., 2013; Natland & Dick, 2001) or new injections of primitive magma (e.g., Bédard et al., 2000; Leuthold et al., 2014), can trigger partial assimilation of the pre-existing mineral matrix and concomitant crystallization of more evolved phases (e.g., Boulanger et al., 2020; Coogan, Saunders, et al., 2000; Gao et al., 2007; Lissenberg & MacLeod, 2016; Lissenberg et al., 2013; Sanfilippo et al., 2020, 2015; Zhang et al., 2020). The process of reactive melt migration is inferred to occur through the connected pores of the crystal mush, and it is thus commonly referred to as "melt reactive porous flow." These reactive processes are able to overprint the geochemical records of magmatic differentiation in early crystallized phases and have a strong effect on the composition of migrating melts (e.g., Lissenberg & Dick, 2008).

Whether the formation of abyssal gabbros involves mainly magmatic crystallization of Mid Ocean Ridge Basalts (MORBs)-type melts or reactive processes in the lower oceanic crust, they show a typical cumulate geochemical signature (e.g., Dick et al., 2019, 2000; Godard et al., 2009). This indicates that gabbros do not represent frozen MORBs; rather, melts must have been extracted from the crystal mush at some stage of its evolution. Melt extraction is considered to occur by compaction of the crystal matrix (e.g., Natland & Dick, 2001; Solano et al., 2014), although lower crustal gabbroic rocks often record little compaction-driven deformation. The high concentration of interstitial melts into melt-rich zones (assisted or not by compaction) may promote an efficient mechanism to collect the residual melts extracted from the crystal mush (Lissenberg et al., 2019). Numerical modeling of melt transport via reactive flow demonstrate that melt accumulation most likely occurs at the top of the igneous body in reservoirs that contain more than 70% melt, in turn favoring melt mobilization and promoting their eruption (Jackson et al., 2018). The mechanisms of melt extraction from deep crystal mushes at slow-spreading ridges are still poorly constrained, and new constraints are required to shed light on melt aggregation processes giving rise to MORB genesis.

A common feature in oceanic olivine gabbros worldwide is the occurrence of grain-size variations (slow-spreading centers: Atlantis Bank OCC, Dick, Meyer, et al., 1991, and Atlantis Massif OCC, Mid-Atlantic Ridge, Blackman et al., 2006, 2011; fast spreading centers: ODP Hole 1256D, France et al., 2009; Koepke et al., 2011; Teagle et al., 2006, and Hess Deep, Gillis et al., 2014). At the Atlantis Bank OCC, the micrograbbros were preliminarily interpreted as representing melt transport channels through crystallizing intrusions (Dick et al., 2000); nevertheless, no detailed investigation on their formation process has been conducted yet. To constrain the melt migration and subsequent extraction of the residual melts, we here investigate the 810 m-long in situ section of lower oceanic crust recently recovered in IODP Hole U1473A at the Atlantis Bank OCC (Dick et al., 2019; MacLeod et al., 2017). In particular, we selected samples of olivine gabbros displaying intense grain-size variations, at different depths throughout the Hole. We perform detailed petrographic characterization and in situ geochemical analyses of mineral phases across grain-size contacts to comprehend the origin of these grain-size variations. We document that fine-grained olivine gabbro (also referred to as microgabbro) represent in situ crystallized melt-rich levels, which testify former collection of melts possibly residual from reactive porous flow processes.

2. Geological Setting and IODP Hole U1473A

The Atlantis Bank, located at 57°E along the ultraslow-spreading SWIR, is a 5 km-high local dome on the eastern wall of the Atlantis II Transform (Figure 1). This raised dome is an Oceanic Core Complex (OCC) exposing massive gabbro on the seafloor, interpreted to result from initial uplift by detachment faulting at the ridge-transform intersection, and subsequently offset during a period of change in the spreading direction (e.g., Baines et al., 2008; Dick, Schouten, et al., 1991).

IODP Hole U1473A was drilled during IODP Expedition 360 (Dick et al., 2019) into the flat summit of the OCC, 2.2 km north northeast of the 1508-m deep Hole 735B (ODP Leg 118 and IODP Leg 176, e.g., Dick
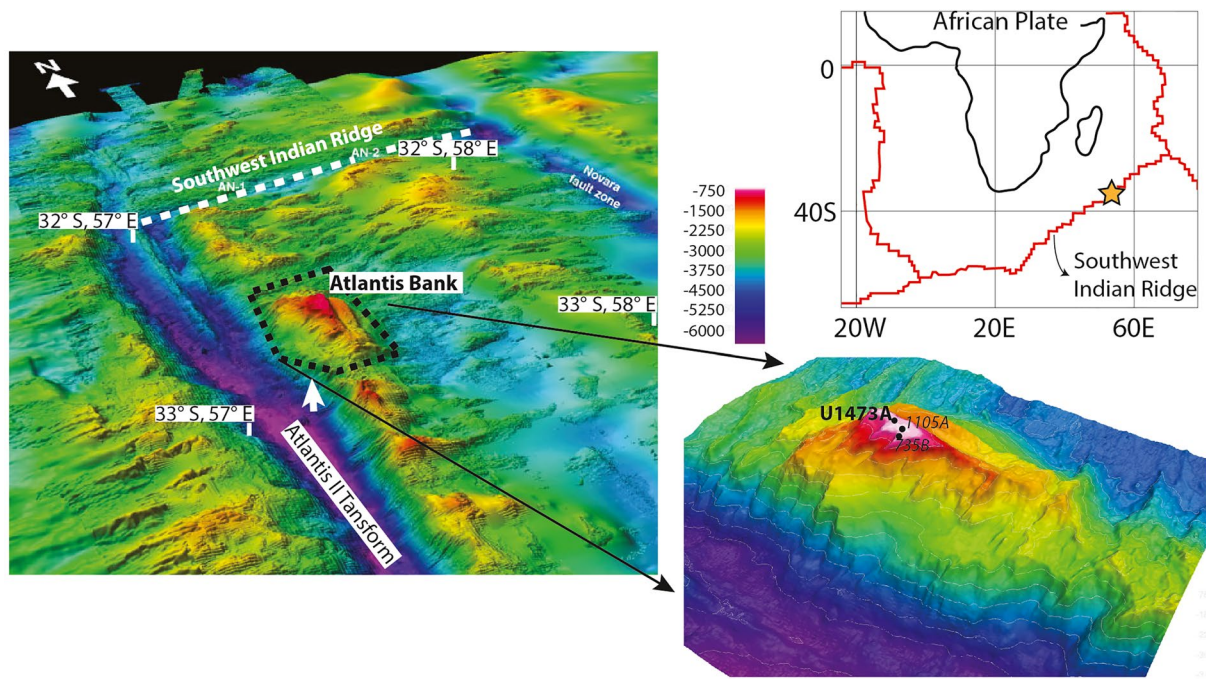
Figure 1. Location of the Atlantis Bank OCC and detailed 3D reconstruction of its dome structure (looking NE) modified after MacLeod et al. (2017). Holes were drilled on the flat top of the dome. In details, Holes 1109A and 735B were drilled during Legs 118 and 176 of the Ocean Drilling Program (e.g., Dick et al., 2000), and Hole U1473A, studied here, during Expedition 360 of the Integrated Ocean Discovery Program.

et al.,2000; Dick, Meyer, et al., 1991). This borehole penetrated ~810 meters below sea floor (mbsf), recovering a section of lower oceanic crust (Figure 2) mainly composed of olivine gabbros (76.5%), less abundant disseminated-oxide gabbro (containing 1%–2% oxide; 9.5% of recovery), oxide gabbro (>5% oxide; 7.5% of recovery), and gabbro (*sensu stricto*; 5% of recovery), and minor felsic veins (1.5%). Two major chemical

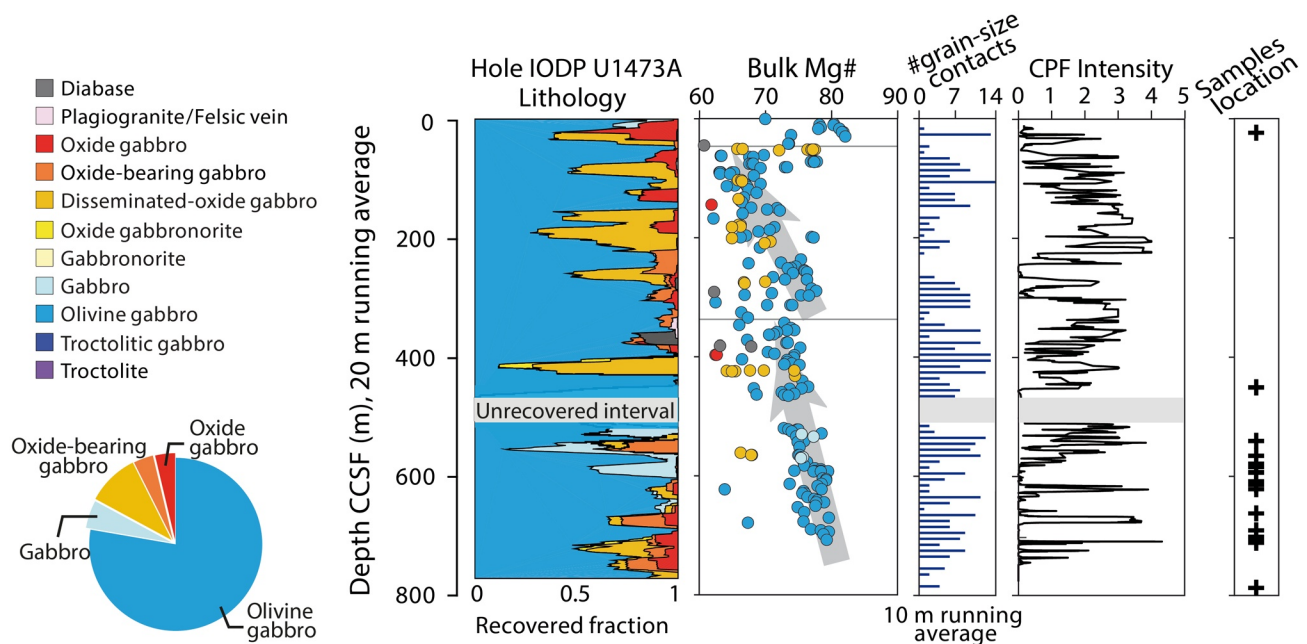**Figure 2.** (From left to right) Pie diagram showing lithologic proportions (vol%) in Hole U1473A; downhole lithostratigraphic variations (relative abundances of rocks are averaged over 20 m) and bulk-rock Mg# (Mg# = 100 × cationic (Mg/(Mg + Fe), with all Fe as Fe2+) of the recovered samples; number of grain size contacts averaged over 10 m; downhole intensity of crystal plastic fabrics; depth of selected samples.
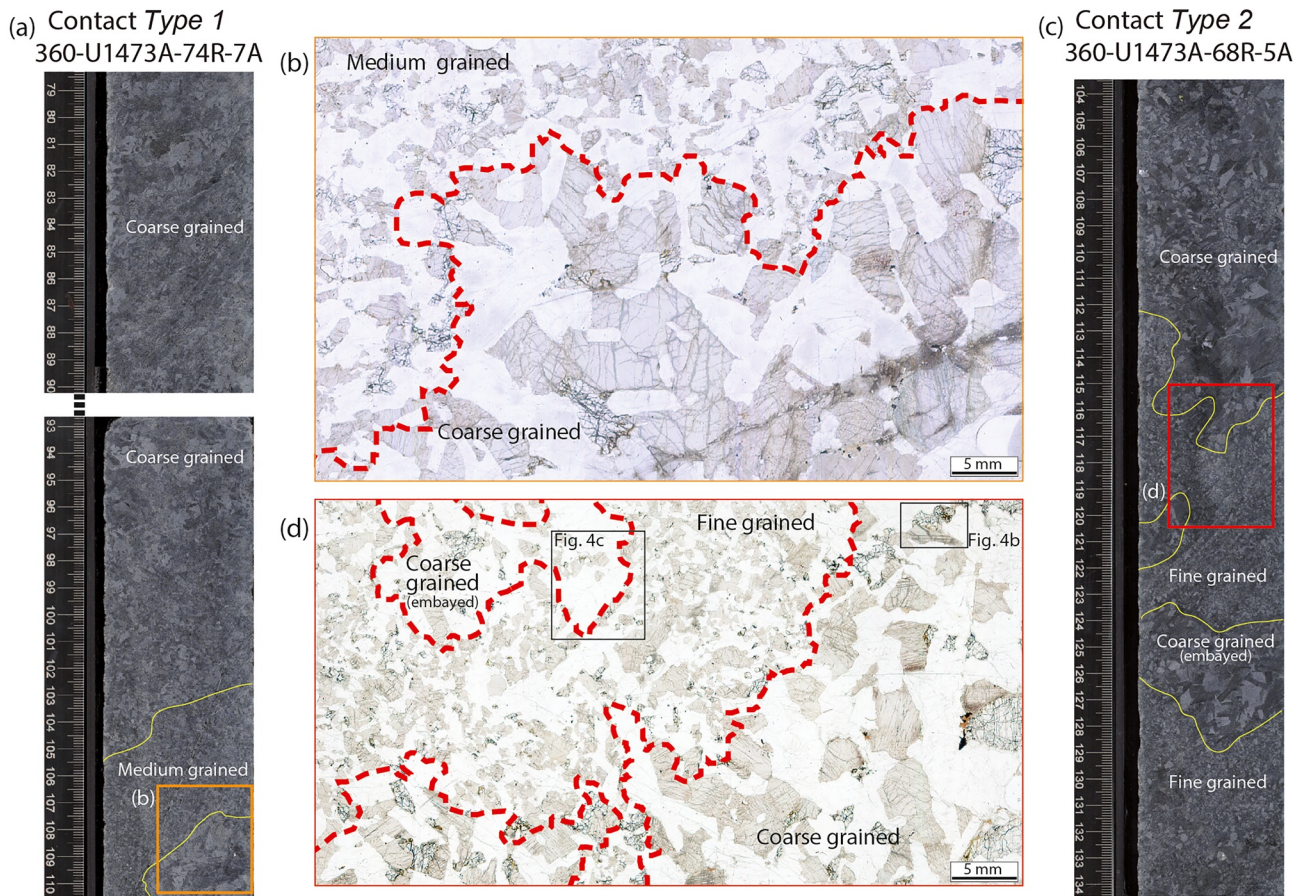
Figure 3. Examples of (a and c) recovered irregular grain-size contacts in U1473A olivine gabbros. (a) Core 74R-7 shows wavy and lobate *Type1* contact with a close-up (orange box) in (b). (c) Core 68R-5 displays sutured and lobate *Type 2* contacts with a close-up (red box) in (d); black boxes locate close-ups of coarse-grained olivine (Figure 4b) and plagioclase (Figure 4c) showing lobate grain boundaries.

discontinuities were identified downhole by Shipboard bulk rock analyses (at ~60–90 mbsf and ~350 mbsf, MacLeod et al., 2017), separating three principal chemical units. Each chemical unit is characterized by gradual upsection decreases in Mg# (Figure 2), Ca#, and Cr and Ni bulk concentrations coupled with increase in Ti and Y contents, similar to chemical trends observed throughout the nearby ODP Hole 735B (Dick et al., 2000). According to Dick et al. (2000), the chemical units in Hole U1473A are interpreted as upward differentiated magmatic intrusive units.

Grain-size of olivine gabbros is highly variable ranging from coarse- to medium- and fine-grained. About 80% of recovered olivine gabbros are coarse-grained, while the remaining 20% are medium- and fine-grained. Primary contacts between intervals of different grain-sizes are copious (121 contacts according to MacLeod et al., 2017; one contact on average every ~4 m of recovered core) and were identified throughout Hole U1473A at all depths (Figure 2). Grain-size variations are mostly irregular and "patchy," that is, showing coarse-grained domains included into a fine-grained matrix, with variable thickness of fine- (or medium-) and coarse-grained intervals (Figure 3; MacLeod et al., 2017). More rarely, the grain-size contacts are sharp, planar and subparallel boundaries that define local igneous layering (Dick et al., 2019). Overall, grain-size contacts are more abundant in the deepest chemical unit (300–800 mbsf; Figure 2) with on average one contact every ~1.5 m.

Throughout Hole U1473A, primary structures and textures are typically variably overprinted by deformation and crystal-plastic fabrics (CPF). The intensity of CPF decreases downhole: between 550 and 800 mbsf primary grain-size variations are well preserved (Figure 2). The strong CPF overprint of the shallowest part of the Hole likely partially prevents the identification of additional grain-size variations.

3. Sample Selection and Analytical Methods

During IODP Expedition 360, rock cores were cut perpendicular to the foliation plane (when visible) and possibly perpendicular to the orientation of grain-size contacts, ideally maximizing the expression of dipping structures on the cut face of the core (MacLeod et al., 2017). Therefore, the observed irregular shapes of grain-size contacts are not 2D-cutting artefacts but are rather real natural features. We sampled fine- and coarse-grained olivine gabbros displaying irregular grain-size contacts at variable depths throughout Hole U1473A. A total of 28 samples were selected: 16 samples across the grain-size contacts and 6 couples (12 samples) within single grain-size intervals, each sampled at 2–~20 cm distance from their respective grain-size contact (Table S1). Of the considered 22 grain-size contacts, 9 are visually sharper and 13 are difficult to delineate and more irregular (*Type 1* and *Type 2*, respectively, as detailed in the following). Representative samples were selected in the least deformed and least altered intervals of the hole and thus mainly within the deepest chemical unit (Figure 2). For comparison with contacts in the upper unit of Hole U1473A, we also sampled a contact at 24 mbsf (360-U1473A-4R-2W, 19–27) and a couple of fine- and coarse-grained olivine gabbros each sampled at ~5 cm distance from their contact located at 450 mbsf (360-U1473A-50R-1W, 73–80 and 360-U1473A-50R-1W, 92–97).

In situ mineral major and trace element analyses were performed across grain-size contacts. We investigated the systematic changes of olivine, plagioclase, and clinopyroxene chemical compositions from the contact into each grain-size interval at increasing distance from the contact.

Minerals major element analyses were performed by Electron Probe Micro Analyzer (EPMA) at Géosciences Montpellier (University of Montpellier), using a CAMECA SX100 equipped with five wavelength-dispersive X-ray spectrometers (WDS). Analyses were conducted with 20 kV accelerating potential, 10 nA beam current and 30 s counting time for all elements measured. Natural minerals and synthetic oxides were used as standards.

Minerals trace element compositions were determined at Géosciences Montpellier, using a Thermo Scientific Element 2XR (eXtended Range) high resolution Inductively Coupled Plasma Mass Spectrometer (ICP-MS). The ICP-MS is coupled with laser ablation (LA) system, a Microlas (Geolas Q +) automated platform with a 193 nm Excimer Compex 102 laser from LambdaPhysik. The laser energy density was set to 12–15 J cm^{-2} and ablation frequency to 10 Hz for analyses of olivine and 8 Hz for plagioclase and clinopyroxene. The laser spot size was set to 77–85 µm. Data were reduced with the GLITTER software package (Van Achterbergh et al., 2001), using the linear fit to ratio method. Concentrations were calibrated against the NIST 612 rhyolitic glass using the values given in Pearce et al. (1997). ^{29}Si for olivine and ^{43}Ca for plagioclase and clinopyroxenes were used for internal standardization relative to EPMA data. Instrument sensitivity related to analytical conditions was determined from the average across all days of repeat measurements of NIST 612. Detection limits were <15 ppm for Ca, between 0.15 and 0.8 ppm for Ti, Cr, Ni and Zn; they were <65 ppb for Mn and Cu, and <25 ppb for Sc, V, Co. Detection limits for the most incompatible elements were <5 ppb except for Rb, Sr, and Ba (<10 ppb). Reference basalt BIR-1G was used as standard to monitor accuracy as well as reproducibility within single series and between runs. This resulted in reproducibility better than 5% for V, Co, Cu, Sr, Nb, Sb, Ba, REE, and it is <15% for all other elements.

4. Contact Characteristics and Textures in Olivine Gabbros

4.1. Irregular Grain-Size Contacts

The irregular and patchy grain-size variations investigated in this study are characterized by: (i) sutured grain-size contacts that are not planar and display variable orientation (Figures 3a and 3c), and (ii) variable thickness of coarse-grained domains embayed in fine-grained olivine gabbro. Based on the thickness of coarse-grained intervals, we distinguish two types of these irregular grain-size contacts that are ubiquitous throughout Hole U1473A and show no systematic distribution downhole (Figure 2 and Table S1).

Type 1 are characterized by coarse-grained intervals (grain size > 4 mm) up to ~60 cm-thick (thickness is estimated considering studied samples only) in contact with variably thick (<20 cm) intervals of medium- (grain size = 1–3 mm) to fine-grained (grain size < 1 mm) olivine gabbro (Figure 3a). Fine-grained domains

are minor in comparison with more common medium-grained intervals. Contacts are sharp but wavy and lobate (Figure 3b).

Type 2 present medium- to fine-grained intervals up to 50 cm-thick, but locally reaching only 2–3 cm-thick, in contact with coarse-grained intervals. The coarse-grained olivine gabbro is locally embayed within the fine-grained intervals in levels less than 10 cm-thick, forming 1 to 2 cm-thick patchy coarse-grained domains (Figures 3c and 3d). Sparsely, single crystals of coarse-grained olivine, plagioclase or clinopyroxene are isolated within fine-grained olivine gabbro. The contacts are often difficult to delineate as the medium- to fine-grained minerals locally appear to crystallize between the coarser-grained minerals (Figure 3d).

Hereafter, both medium- and fine-grained crystals and olivine gabbros are referred to as "fine-grained."

4.2. Magmatic Textures

Olivine gabbros from IODP Hole U1473A contain cumulus assemblages of subhedral to anhedral olivine (0.2–1.5 mm in fine-grained intervals and 2–8 mm in coarse-grained intervals), euhedral and subhedral to lath-shaped plagioclase (0.2–1.5 mm in fine-grained intervals and 1.5–10 mm in coarse-grained intervals), and poikilitic to interstitial clinopyroxene (0.2–1.5 mm in fine-grained intervals and 2–15 mm in coarse-grained intervals), locally enclosing plagioclase ± olivine chadacrysts.

Textures of coarse-grained olivine gabbro are predominantly subophitic with subhedral tabular plagioclase partly or fully enclosed within poikilitic clinopyroxene (Figure 4a). Plagioclase chadacrysts and coarse-grained crystals display magmatic twins, and also show mechanical twins and local undulose extinction indicative of incipient crystal plastic deformation. They have lobate grain boundaries against clinopyroxene. Olivines are deformed and show kink bands. Locally, olivines display corroded contacts against adjacent interstitial clinopyroxene (Figure 4b) and fine-grained plagioclase as well. Large oikocrysts of clinopyroxenes show little undulose extinction, thus indicating that they are slightly deformed.

Fine-grained olivine gabbros are characterized by granular textures (Figure 4c). Plagioclases are euhedral to subhedral (Figures 4c and 4d) and are characterized by the scarce occurrence of mechanical twins (Figure 4c). Olivines mainly appear as subhedral to anhedral undeformed crystals. Clinopyroxenes occur as subhedral crystals and locally enclose subhedral plagioclase (Figure 4d) ± olivine; they display little undulose extinction.

At grain-size contacts, coarse-grained plagioclase displays lobate grain boundaries against fine-grained minerals (Figure 4c). Poikilitic coarse-grained clinopyroxene can be found in optical continuity with the interstitial clinopyroxene within the fine-grained olivine gabbro (Figure 4d), thus indicating that they are a single crystal. On the other hand, fine-grained plagioclase is never found in optical continuity with the coarse-grained counterpart and always occurs as new nuclei.

5. Mineral Compositions

Representative major, minor, and trace element compositions of olivine, plagioclase, and clinopyroxene are reported in Table S2. In the following, we present the overall mineral compositions of fine-grained and coarse-grained crystals.

5.1. Major and Minor Elements

Minerals from olivine gabbros in Hole U1473A have major element compositions comparable with compositions of olivine, plagioclase and clinopyroxene from ODP Hole 735B (Boulanger, 2020; Boulanger et al., 2020; Dick et al., 2002; Sanfilippo et al., 2020; Zhang et al., 2020; Figures 5 and 6).

Olivine crystals show no systematic core-to-rim chemical variations. Overall, they have homogeneous compositions within single grain-size intervals, but vary with no systematic correlations throughout the Hole. Coarse-grained olivine has Mg# ranging on average from 66 to 76 mol% (average per sample in Figure 5), low compatible elements (Ni = 375–680 ppm, Co = 180–222 ppm) and high moderately incompatible elements (Mn = 2314–3,402 ppm, Zn = 84–155 ppm). Mainly across *Type 1* contacts, fine-grained olivines
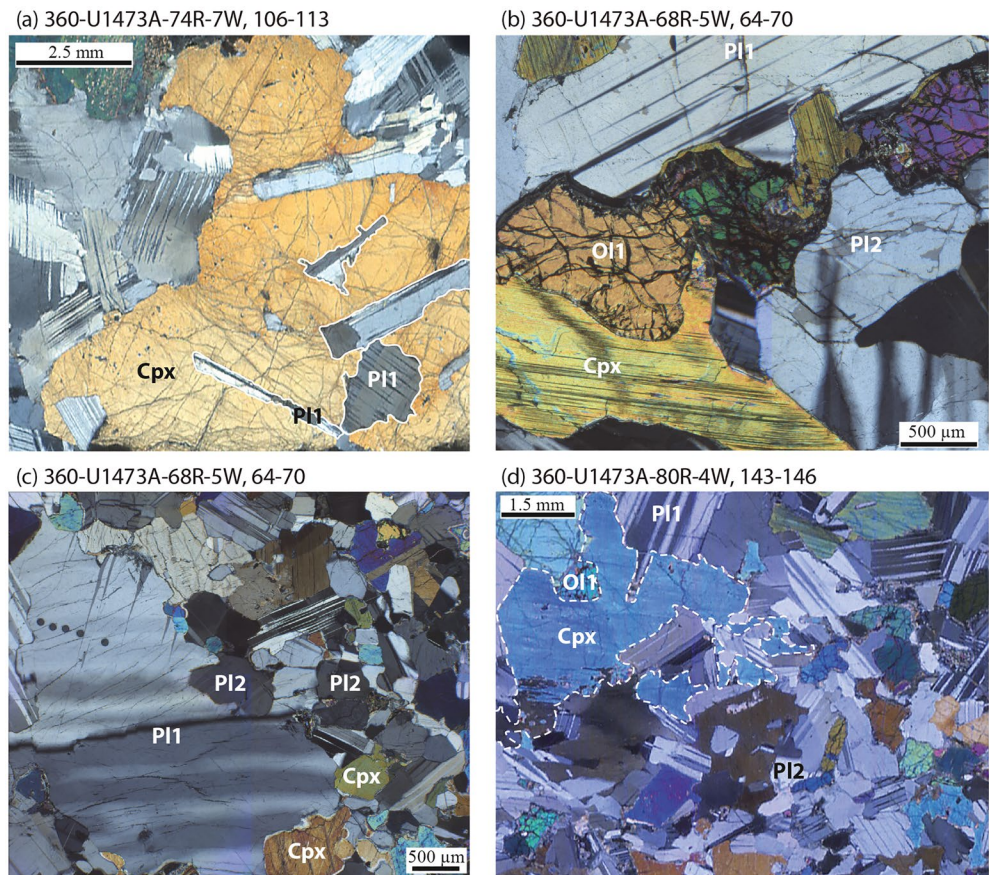
Figure 4. Textural variability in (a and b) coarse-grained olivine gabbro and (c and d) coarse- to fine-grained olivine gabbro from IODP Hole U1473A. Name of samples are noted on top of each photomicrograph (cross polarized light). (a) Large poikilitic clinopyroxene oikocryst embay plagioclase showing corroded grain boundaries. (b) Coarse-grained plagioclase and olivine display lobate grain boundaries against interstitial and locally vermicular clinopyroxene. (c) Coarse-grained plagioclase displays corroded grain boundaries at contact with fine-grained crystals (mostly plagioclase and clinopyroxene). (d) Coarse-grained clinopyroxene at contact with fine-grained material is in optical continuity with fine grained clinopyroxene indicating that they constitute the same single crystal.

display slightly lower contents in compatible elements, but similar moderately incompatible elements compared to coarse-grained olivines. All olivines display remarkably low Ca contents (Ca = 105–563 ppm), with the fine-grained olivine showing the lowest values.

Plagioclase crystals have An contents ranging on average from 56 to 64 mol% (average per sample in Figure 5). Coarse-grained plagioclases exhibit a typical chemical zoning, marked by the decrease in An contents from the crystal cores to their rims. Fine-grained plagioclase is unzoned. Chemical heterogeneity between fine- and coarse-grained plagioclase are exclusively observed at the scale of single grain-size contacts, more specifically in Type 1 contacts. There, cores of coarse-grained plagioclase display higher An contents compared to their relative rims, which have compositions comparable to unzoned fine-grained crystals.

Clinopyroxene crystals show the most heterogeneous composition among all phases (Figures 5 and 6) with a wide compositional range of Mg# (72–86 mol%, Figure 5), but rather comparable Cr_2O_3 contents between crystal cores and rims (Figure 6a). Exception is made for some crystal cores displaying higher Cr_2O_3 contents compared to their relative rims (Figure 6a). Coarse-grained clinopyroxenes display an evident chemical zoning characterized by a decrease in Mg# (79–86 mol% at crystal cores to 76–82 mol% at rims; Figure 5), Al_2O_3 (2.93 ± 0.70 wt% to 2.62 ± 0.60 wt%; Figure 6b) and Ni contents (109 ± 19 ppm to 94 ± 14 ppm) coupled with an increase in TiO_2 (from 0.55 ± 0.25 wt% to 0.91 ± 0.30 wt%; Figures 6c and 7) from the cores to the rims of the crystals. Notably, at a given olivine Mg#, cores of coarse-grained
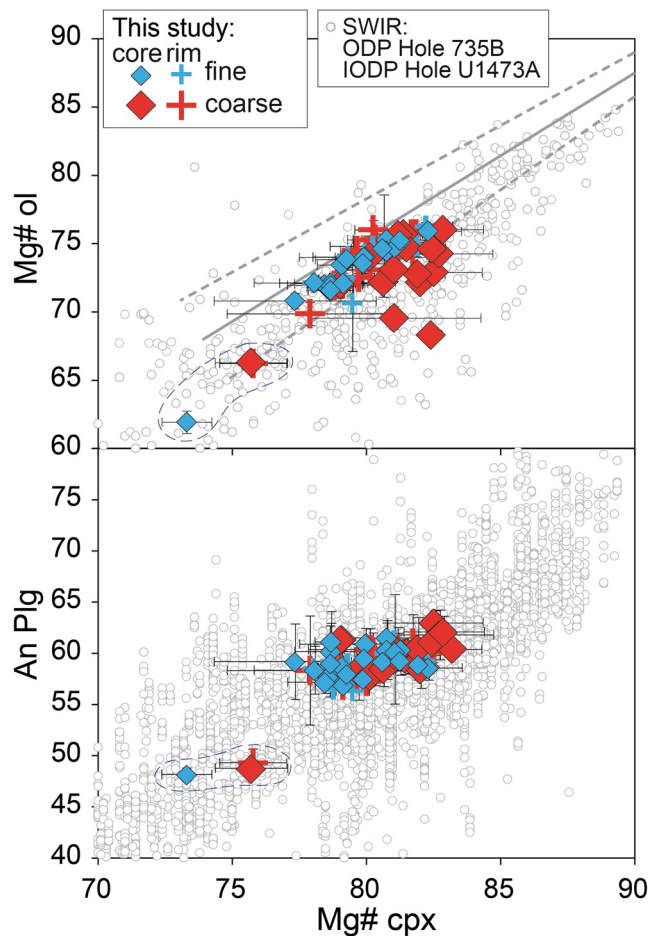
Figure 5. Coarse- (red) and fine-grained (blue) clinopyroxene Mg# (Mg# = 100 × cationic (Mg/(Mg + Fe)) versus olivine Mg# and An content in plagioclase (average mineral composition per sample) from the studied olivine gabbros. Data are compared with theoretical Fe–Mg equilibrium between olivine and clinopyroxene, assuming mineral-melt Fe–Mg partition coefficients of 0.30 for olivine and 0.23 for clinopyroxene (Roeder & Emslie, 1970). The dashed lines represent the calculated olivine–clinopyroxene equilibrium line assuming an uncertainty of ±0.02 on the mineral–melt partition coefficients. Compositions of clinopyroxene-olivine and clinopyroxene-plagioclase in olivine gabbros from the nearby recovered ODP Hole 735B (Boulanger et al., 2020; Dick et al., 2002) and recent data from IODP Hole U1473A (Boulanger, 2020; Sanfilippo et al., 2020; Zhang et al., 2020) are reported for comparison. The dashed circles highlight the most evolved mineral compositions in sample 360-U1473A-83R-4W, 118–124 cm.

clinopyroxene have Mg# higher than the predicted composition of clinopyroxene in equilibrium with coexisting olivine (Figure 5). Fine-grained clinopyroxenes are chemically unzoned, and share similar compositions with rims of coarse-grained crystals (Figures 5 and 6).

Sample 360-U1473A-83R-4W, 118–124 cm displays the most evolved mineral compositions (Mg#$_{ol}$ = 61–66 mol%, An = 48–51, Mg#$_{cpx}$ = 72–76) among all olivine gabbros from this study (Figure 5), testifying the local variability in mineral compositions throughout the Hole. Their in-sample chemical variability is related to the zonation of coarse-grained crystals, and to the more evolved signature of fine-grained minerals compared to the adjacent coarse-grained minerals.

5.2. Trace Elements

Minerals trace element contents display different in-sample geochemical heterogeneity, that is, *Type 1* and *Type 2* contacts can be distinguished by distinct variations in mineral compositions across the contacts. Overall, *Type 1* contacts are characterized by marked geochemical variations between coarse- and fine-grained minerals, while *Type 2* contacts display minor geochemical heterogeneity (Figure 7, Figures S1 and S2). Here we describe the mineral trace element compositions of all analyzed phases regardless of the type of contact; the detailed discussion about geochemical heterogeneity across the two types of contacts will be given in the Discussion (Section 7.3).

Olivines are on average depleted in lithophile trace elements (Figures S1, S2a, and S2b in Supplementary Material). They display strong normalized H (heavy)–REE to M (medium)–REE fractionations (Dy$_N$/Yb$_N$ = 0.02–0.12, Figure S1). Olivines show strong enrichments in the most incompatible High Field Strength Elements (HFSE), such as Ti and Zr-Hf, relative to elements with similar partition coefficients during mantle melting (hereafter, referred to as "neighboring trace elements" in spider diagrams; Figures S2a and S2b). These enrichments and the HREE to MREE fractionations of the studied olivines are similar to those observed in olivines modified during melt reactive porous flow in gabbroic rocks from ophiolitic massifs (e.g., Alpine ophiolites; Basch et al., 2018; Rampone et al., 2016; Sanfilippo et al., 2014) and oceanic crustal sequences from slow-spreading oceanic centers (e.g., IODP Hole U1473A and ODP Hole 735B; Boulanger, 2020; Boulanger et al., 2020; Atlantis Massif OCC; Drouin et al., 2009; Ferrando et al., 2018). Cores of coarse-grained olivine have on average higher MREE, HREE, and HFSE concentrations compared to cores of fine-grained olivine (Figures S1 and S2a). Both fine- and coarse-grained olivines are geochemically unzoned (Figures S1 and S2b), although some rims of coarse-grained olivine show lower MREE, HREE, and HFSE contents than their relative cores (Figures S1 and S2b).

Plagioclases display prominent positive Eu anomalies (Eu/Eu* = 10–31; Figures 7a and 7b). L (light)–REE contents (Ce$_N$ = 0.65–4.66) vary in a range comparable with compositions of plagioclase in olivine gabbros from the Kane area (MAR, MARK area; Ce$_N$ = 0.47–5.42; Coogan, Kempton, et al., 2000; Coogan, Saunders, et al., 2000). Trace element patterns show positive anomalies in Sr and Ti relative to neighboring elements, and negative anomalies in Zr (Figures S2c and S2d). Coarse-grained plagioclases show zoning in trace elements marked by an overall increase in concentrations toward the crystal rims, which is in accord with their major element signature. Although zonation of coarse-grained plagioclases in major and trace elements recall a magmatic differentiation trend, the enrichments in trace elements cannot be reproduced by pure fractional crystallization process (Figure S3a). Specifically, crystal cores display nearly flat
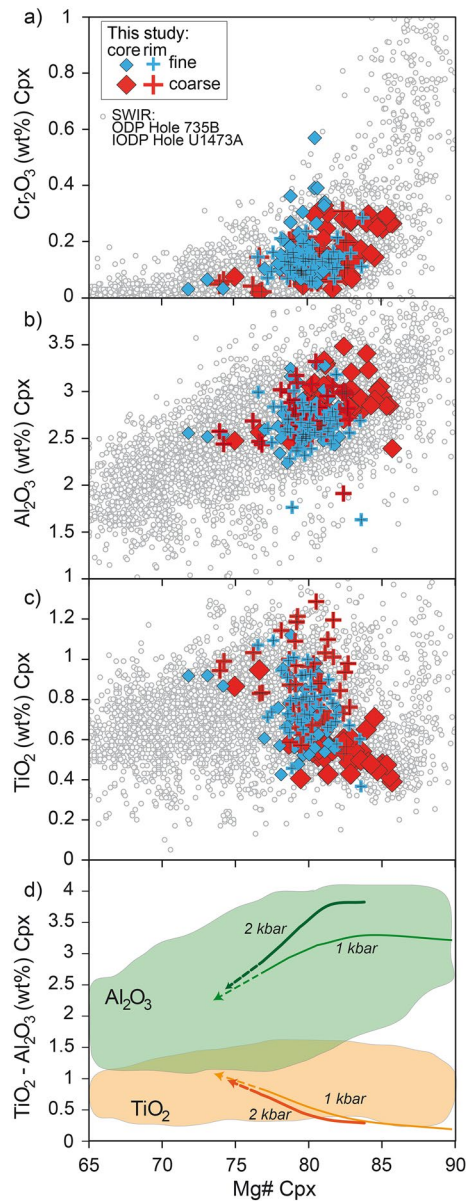
Figure 6. Clinopyroxene major element compositions in coarse- (red) and fine-grained (blue) intervals: Mg# versus (a) Cr_2O_3 (wt%), (b) Al_2O_3 (wt%), and (c) TiO_2 (wt%). uncertainty of ±0.02 on the mineral–melt partition coefficients. Compositions of clinopyroxenes from the nearby recovered ODP Hole 735B (Boulanger et al., 2020; Dick et al., 2002) and recent data from IODP Hole U1473A (Boulanger, 2020; Sanfilippo et al., 2020; Zhang et al., 2020) are reported for comparison. (d) Al_2O_3 (wt%; in green) and TiO_2 (wt%; in orange) clinopyroxene lines of descent for crystallization at 2 kbar (dark-thick lines) and 1 kbar (light-thin lines); clinopyroxene chemical evolution is predicted by crystallization experiments of a tholeiitic basalt with the composition of a microgabbro from Hole 735B (Feig et al., 2006).

LREE patterns (Ce_N = 0.65–4.11) and rather low LREE to MREE fractionations (Ce_N/Sm_N = 1.28–3.64; Figure 7a), whereas rims have higher LREE contents (Ce_N = 0.96–4.66) leading to stronger REE fractionations (Ce_N/Sm_N = 1.32–5.48; Figure 7b). Fine-grained plagioclases are unzoned and show trace elements compositions similar to rims of coarse-grained plagioclase (Figure 7b, Figures S2c and S2d).

Clinopyroxenes have nearly flat patterns for MREE and HREE (Yb_N = 6.9–34.4), and variable depletion in LREE (Figures 7c and 7d). Their REE contents are similar, but reach more evolved compositions compared to the composition of clinopyroxenes in olivine gabbros from the MARK area (Yb_N = 7.2–10.9; Coogan, Kempton, et al., 2000; Coogan, Saunders, et al., 2000). All clinopyroxenes are distinguished by moderate negative anomalies in Ti, while contents of Zr-Hf are significantly variable from depleted to enriched relative to neighbor trace elements (Zr_N/Nd_N = 0.42–1.85). Negative anomalies are also observed for Sr and Pb on extended trace element patterns (Figures S2e and S2f). Coarse-grained clinopyroxenes display zoning in trace elements characterized by an overall increase in concentrations toward the crystal rims, which is in agreement with their major element signature. As observed in coarse-grained plagioclase, this geochemical zoning cannot be reproduced by a pure fractional crystallization process (Figure S3b). In detail, crystal cores have low trace elements contents (Yb_N = 6.9–17.1 ppm, Figure 7c; Zr = 7.4–40.3 ppm, Figures S2e and S3b) and display fractionated patterns of LREE to Y (Ce_N/Y_N = 0.18–0.43) and no to little Eu negative anomalies (Eu/Eu* = 0.81–1.02). Rims of coarse-grained crystals exhibit a pronounced Eu negative anomaly (Eu/Eu* = 0.55–0.84), and enrichments in the most incompatible elements (Ce_N = 2.3–17.4, Figure 7d; Zr = 9.8–101.1 ppm, Figure S2f) compared to the least incompatible (Y_N = 8.1–28.4, Figure 7d; Nd = 2.1–7.5 ppm, Figure S2f). These trace elements concentrations are typically reported in clinopyroxene from other olivine gabbros from Hole 735B (Gao et al., 2007; Lissenberg & MacLeod, 2016) and result in increasing trace elements fractionations from the cores (Zr_N/Nd_N = 0.42–0.89; Figure S2e) to the rims (Ce_N/Y_N = 0.23–0.87 and Zr_N/Nd_N = 0.42–1.17; Figure S2f) of the crystals. Fine-grained clinopyroxene are overall unzoned and have compositions similar to the rims of coarse-grained clinopyroxene (Figure 7d, Figure S2f).

6. Equilibrium Temperatures

Plagioclase-clinopyroxene and olivine-clinopyroxene equilibrium temperatures were computed to investigate temperatures of magmatic processes recorded in olivine gabbros from Hole U1473A. Temperatures were determined using two geothermometers based on partitioning of REE between the two mineral pairs considered. The geothermometer from C. Sun et al. (2017) was used for plagioclase-clinopyroxene pairs, while the geothermometer from C. Sun and Liang (2012, 2013, 2014) for olivine-clinopyroxene. Because LREE and MREE contents in olivine are close to the detection limit, and thus to avoid the analytical error, we considered only HREE and Y for calculation of the olivine-clinopyroxene equilibrium temperatures.

Equilibrium temperatures between plagioclase and clinopyroxene range in the interval 1050 °C–1160 °C (±50 °C; Figure 8). The highest temperatures are recorded in pairs of coarse-grained crystal cores (1100 °C–1160 °C) and decrease toward fine-grained crystal cores (1060 °C–1090 °C). Equilibrium temperatures
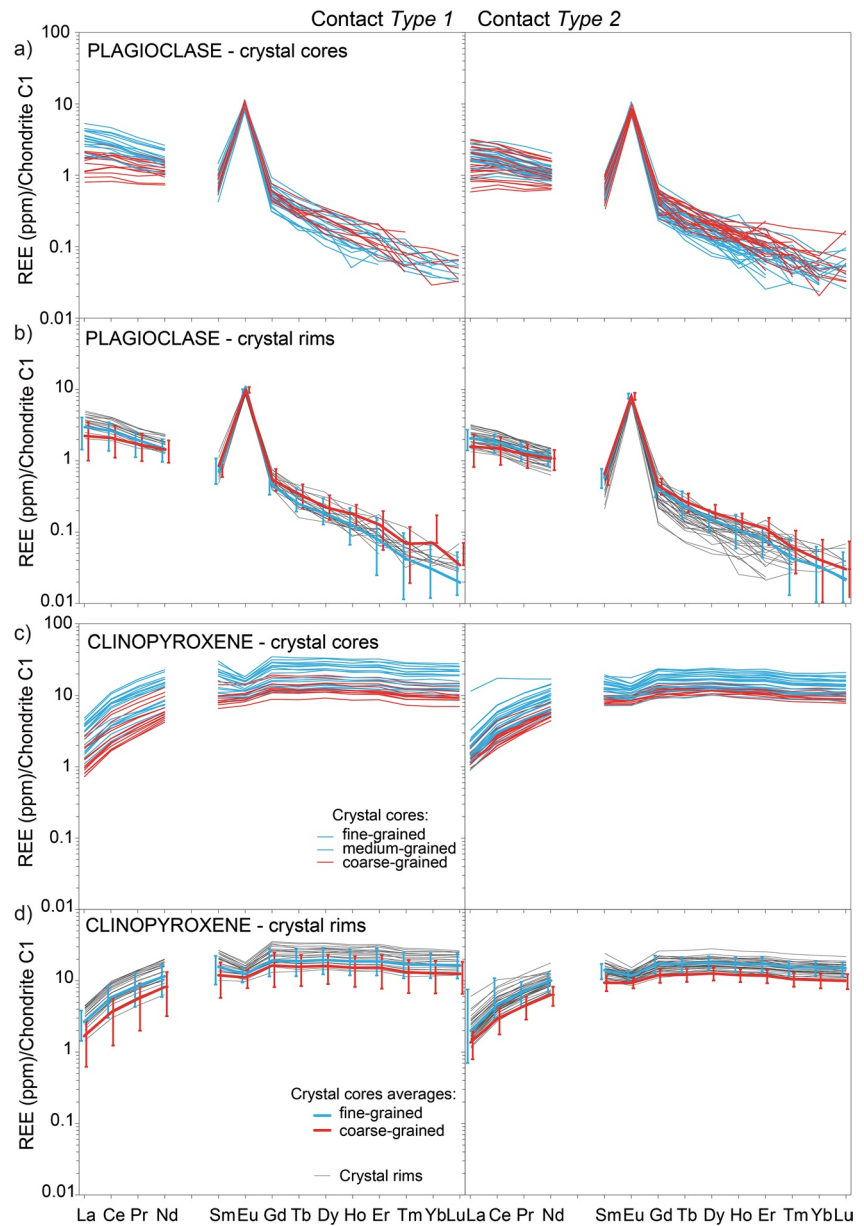
Figure 7. Chondrite-normalized Rare Earth Element (REE) concentrations of plagioclase (a and b) and clinopyroxene (c and d) from U1473A olivine gabbros characterized by *Type 1* (left column) and *Type 2* (right column) grain-size contacts. In (a) and (c) we plot compositions of crystal cores; in (b) and (d) average compositions of crystal cores (colors refer to the size of crystals: coarse in red, and fine in blue) are compared with crystal rims (gray lines). Colored bars in (b) and (d) indicate the single-element compositional range of crystal cores. Normalizing values are after S.-s. Sun and McDonough (1989).

calculated using compositions of crystal rims vary in a narrower range with no systematic variations (1070 °C–1105 °C). The latter are within-error similar to temperatures measured at cores of fine-grained crystals, and thus lower than the one obtained from cores of coarse-grained crystals. Our equilibrium temperatures are comparable with temperatures estimates from olivine gabbros in the nearby ODP Hole 735B (Boulanger et al., 2020). In particular, temperature estimates from rims of coarse-grained and unzoned fine-grained clinopyroxene-plagioclase pairs overlap with equilibrium temperatures from the most evolved olivine gabbros in the lower crustal section at the Atlantis Bank OCC.
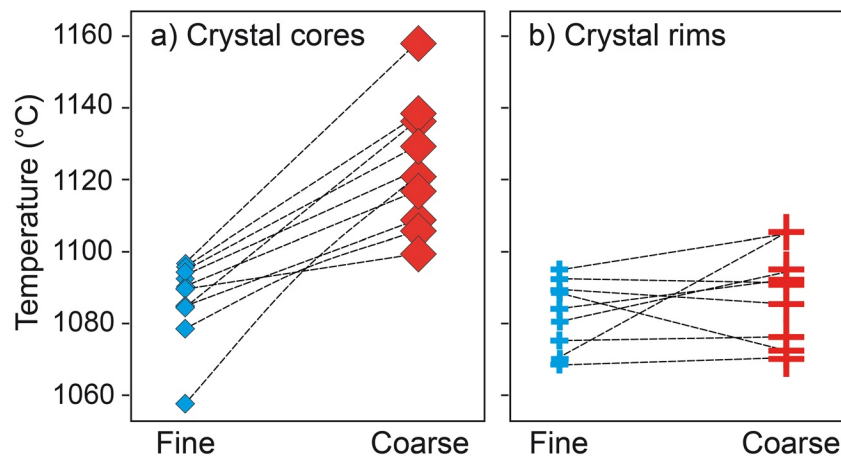
Figure 8. Equilibrium temperatures recorded in plagioclase-clinopyroxene pairs. Temperatures were calculated between cores (a) and rims (b) of coarse- (red) and fine-grained (blue) crystals, using the geothermometer from C. Sun et al. (2017). Colors and symbols are as in Figures 5 and 6.

Equilibrium temperatures between olivine and clinopyroxene are overall lower than 1000 °C (Figure S4), thus suggesting chemical re-equilibration of trace element in olivine under subsolidus conditions (C. Sun & Liang, 2014). The lower MREE, HREE, and HFSE contents at the rims of some coarse-grained olivine compared to their cores is consistent with element redistribution and diffusion from the olivine crystal to the adjacent mineral phases (mainly clinopyroxene; C. Sun & Liang, 2012, 2013, 2014). Also, the absence of zonation in fine-grained olivines showing on average the lowest trace element contents is in line with complete re-equilibration during cooling, which is documented to be achieved more rapidly over shorter distances (e.g., Coogan et al., 2007 and references therein). Re-equilibration at subsolidus conditions is further indicated by the very low Ca contents in the studied olivines, which point to Ca redistribution from olivine into clinopyroxene during cooling of the oceanic crustal sequence (e.g., Coogan et al., 2007, 2005; Faak & Gillis, 2016; Ferrando et al., 2020). Thus, equilibrium temperatures and the geochemical signature of olivine in the olivine gabbros from Hole U1473A indicate that the primary magmatic composition of olivine was modified during exhumation and cooling of the crustal sequence. For this reason, only plagioclase and clinopyroxene compositions are considered in the following discussion.

7. Discussion

7.1. Assessing the Dominant Magmatic Process Forming the Olivine Gabbro

7.1.1. A Pure Magmatic Crystallization Process?

The poikilitic textures of coarse-grained olivine gabbros are characterized by large oikocrysts of clinopyroxene embaying chadacrysts of plagioclase ± olivine (Figure 4a). These relationships may recall primary cumulus textures resulting from the solidification of slowly cooled mafic crystal mushes (e.g., Holness et al., 2007; Nielsen et al., 2015). The studied fine-grained olivine gabbros are characterized by granular textures (Figure 4c) likely resulting from in situ adcumulus growth (e.g., O'Driscoll, 2005). Both poikilitic and granular minerals may form during pure magmatic crystallization of various magma pulses in a magmatic body, where minerals are unmodified after crystal accumulation (e.g., Holness et al., 2015). Overall, in the gabbros from the Atlantis Bank OCC (this study; Boulanger et al., 2020; Dick et al., 2002; Sanfilippo et al., 2020; Zhang et al., 2020), the decrease in clinopyroxene Mg# coupled with a decrease in olivine Mg# and An in plagioclase (Figure 5), together with the decrease in Cr_2O_3, Al_2O_3, and TiO_2 in clinopyroxene at decreasing Mg# (Figure 6), may be reproduced at first order by pure fractional crystallization at rather low pressures (Figure 6d).

Although textures and mineral major element compositions suggest a common crystallization process, minor and trace element compositions of minerals call for the involvement of additional magmatic processes. The coarse-grained olivine gabbro selected for the present study exhibits clinopyroxene and plagioclase
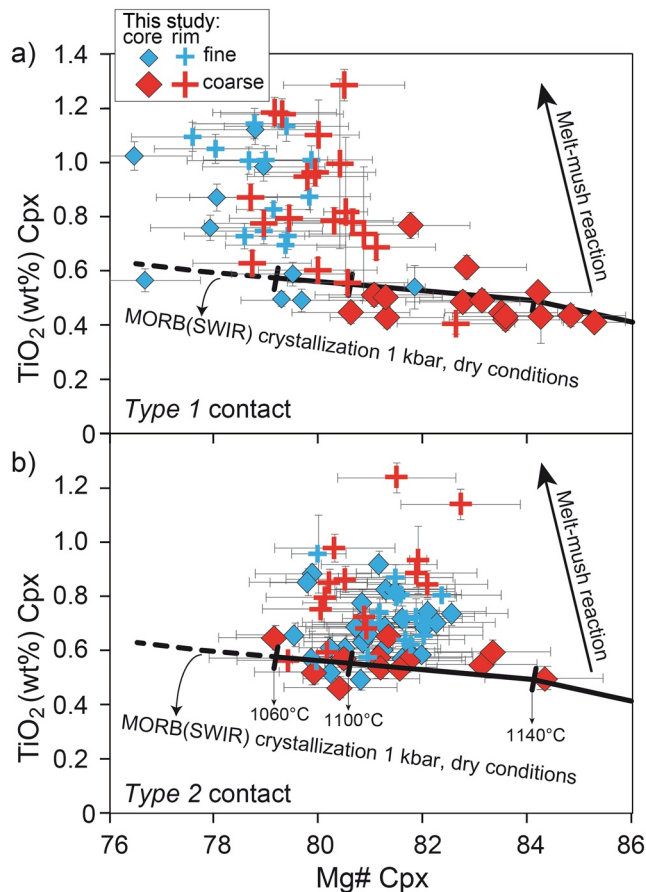
Figure 9. Mg# versus TiO$_2$ (wt%) of clinopyroxene in a representative sample of *Type 1* (a) and *Type 2* (b) grain-size contacts. Notice the heterogeneous clinopyroxene compositions across *Type 1* contact (more primitive cores of coarse-grained crystals to more evolved rims and unzoned fine-grained crystals), whereas clinopyroxenes across *Type 2* contact are homogeneous. We report for comparison variations in clinopyroxene compositions during: (i) melt-mush reaction reproduced in reactive crystallization experiments of a primitive MORB percolating through a troctolite (Yang et al., 2019); (ii) crystallization experiments of a tholeiitic basalt with composition corresponding to a microgabbro from Hole 735B at 1 kbar (Feig et al., 2006).

geochemical zoning. From the core to the rim of clinopyroxene, compatible elements decrease (e.g., Mg# and Cr; Figures 5 and 6), Sr and Eu anomalies deepen, and incompatible elements increase (Figure 7, Figure S2). With respect to plagioclase core, the rims are enriched in LREE, and slightly depleted in HREE and Y (Figure 7). Notably, crystal rim compositions display enrichments in some of the most incompatible elements, such as Zr in clinopyroxene and Ce in plagioclase (Figure S3), thereby leading to stronger fractionations of most/less incompatible elements, namely Ce$_N$/Y$_N$ and Zr$_N$/Nd$_N$ in clinopyroxene and Ce$_N$/Y$_N$ and Ce$_N$/Sm$_N$ in plagioclase (Figure S5). Ti is also remarkably enriched at the rims of clinopyroxene crystals (Figure 6c), especially at Type 1 contacts (Figure 9). These minor and trace element enrichments exceed values predicted for pure crystallization at (low) pressures assumed for gabbros formation beneath slow-spreading ridges (e.g., Feig et al., 2006; Grimes et al., 2008; Kelley & Fruh-Green, 2001; Vanko & Stakes, 1991; Figure 9; Figures S3 and S5).

Enrichments in incompatible elements at crystal rims were described in plutonic gabbroic rocks (e.g., Bédard et al., 2009), and their origin was ascribed to the entrapment of small aliquots of melt within a crystal matrix as the system cools (see also Bédard, 1994; Elthon et al., 1992; Meyer et al., 1989). To assess the potential contribution of trapped melt crystallization in selected olivine gabbros, we used the Equilibrium Distribution Method (EDM; Bédard, 1994; Bédard et al., 2009) to model the geochemical evolution of clinopyroxene during late-stage crystallization in a closed system. We considered the bulk and mineral compositions of a sample (U1473A-68R-5-W, 103–110 cm) showing a marked mineral zoning (Figures S6a and S2b; see figure caption for further details of the model parameters). Based on the modal composition, the proportion of crystallizing phases was set to 5% olivine, 60% plagioclase and 35% clinopyroxene, and the trapped melt fraction was assumed to vary between 20% and 0.5%. The entrapment of low amounts of trapped melt (<2%; Figures S6a and S2b) can increase both the elemental concentrations and the fractionations of most/less incompatible element ratios. However, the model is not able to reproduce the observed crystal rim compositions (Figures S6a and S6b). In addition, the process of extreme melt fractionation (i.e., marked decrease in melt mass down to ~2% of the initial melt mass) leads to saturation in Fe-Ti oxide phases, orthopyroxene and amphibole (Feig et al., 2006; Koepke et al., 2018), which are not observed in the studied olivine gabbros. We conclude that fractional crystallization coupled with melt entrapment in a closed system is not the dominant process forming the Hole U1473A olivine gabbros.

In an alternative petrogenetic hypothesis, Langmuir (1989) proposed that enrichments in incompatible elements in minerals from a continental layered intrusion resulted from "in situ crystallization." The latter involves crystallization at the margins of a magma chamber and return of the remaining melt fraction into the chamber interior. This process was also considered to explain the global incompatible trace element over-enrichment observed in MORBs (Coogan & O'Hara, 2015). We tested the ability of in situ crystallization to reproduce the trace element enrichments observed at the crystal rims in samples selected for the present study, by using the equation proposed by Langmuir (1989) (Figures S6c–S6f; see figure caption for further details on the model parameters). Trends of in situ crystallization were simulated for different aliquots of melt returning in the magma chamber interior (*f* = 0.1 and 0.2; Figures S6c–S6f). They predict increasing REE concentrations in the crystallizing phases as melt fractionates, and reproduce a minor range of most/less incompatible element fractionations of analyzed clinopyroxene and plagioclase grains. However, even

considering the most fractionated melt returning to the magma chamber (f = 0.1), the model fails to reproduce the highest trace element fractionations observed for clinopyroxene and plagioclase (Figures S6c–S6f).

In summary, magmatic crystallization, including processes of pure fractional crystallization (Figures S3 and S5) and in situ crystallization (Figures S6c–S6f), may be considered as a plausible process forming the cores of coarse-grained minerals. However, it fails to simulate the marked over-enrichments in the most incompatible elements compared to the least incompatible elements observed for clinopyroxene-plagioclase pairs in selected coarse-grained olivine gabbros. We emphasize that a process of melt entrapment in a closed system implies a process of late-stage crystallization (F < 20%; Figures S6a and S6b), which is not consistent with the formation of crystal cores representing, in the case of the studied lower oceanic crustal sequence, early crystallized melt fraction (F ∼80%). We conclude that another magmatic process must be invoked, likely occurring after crystallization of primary crystal cores.

7.1.2. A Reactive Crystallization Process Producing Trace Element Over-Enrichments
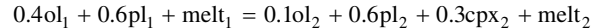
The studied coarse-grained olivine gabbros display remarkable irregular shape and resorbed grain boundaries of the plagioclase chadacrysts (Figure 4a). Locally, olivine also displays resorbed grain boundaries against interstitial to poikilitic clinopyroxene (Figure 4b). These textural features resemble those of olivine gabbros from other sections of slow-spreading oceanic crust that locally experienced dissolution-precipitation processes, involving olivine and plagioclase dissolution by a melt that precipitated clinopyroxene (e.g., Boulanger et al., 2020; Lissenberg & Dick, 2008; Lissenberg & MacLeod, 2016; Sanfilippo et al., 2015). Chemical disequilibrium in olivine-clinopyroxene Mg# is also commonly documented in dissolution-precipitation textures, indicating olivine partial assimilation prior to clinopyroxene crystallization (e.g., Basch et al., 2019; Coogan, Saunders, et al., 2000; Drouin et al., 2009; Ferrando et al., 2018; Lissenberg & Dick, 2008; Sanfilippo et al., 2013, 2015). Consistently, the cores of coarse-grained clinopyroxenes from the studied olivine gabbros have higher Mg# (∼82–84 mol%) compared to the calculated Mg# of clinopyroxene (∼80–82 mol%) in equilibrium with coexisting olivine with Mg# ∼72–74 mol% (Figure 5). Interestingly, at the Atlantis Bank OCC, cryptic variations in mineral major element compositions (database reported by Dick et al., 2002) have been interpreted as re-equilibration of a crystal mush with melts percolating by permeable flow (Dick et al., 2002).

Intra-crystalline trace element zoning has been described in most gabbroic sequences (e.g., Basch et al., 2018; Borghini & Rampone, 2007; Boulanger et al., 2020; Coogan, Saunders, et al., 2000; Drouin et al., 2009; Ferrando et al., 2018; Gao et al., 2007; Lissenberg & MacLeod, 2016; Lissenberg et al., 2013; Sanfilippo et al., 2015, 2020; Tribuzio et al., 2000; Zhang et al., 2020). Typically, trace element concentrations from the crystal cores to the rims are marked by a preferential increase in the most incompatible elements (Zr, Hf, LREE) compared to less incompatible elements (M-HREE, Y), as those observed in this study (see comparison in Figure S5). Remarkable Zr_N/Nd_N positive anomalies in clinopyroxene (see Figure S2f) have been described in gabbroic sequences as marker of mineral-melt interactions (e.g., Borghini & Rampone, 2007). Specifically for gabbros from the Atlantis Bank OCC, several authors have suggested that these mineral zoning can result from assimilation of the pre-existing gabbroic minerals and concomitant crystallization of new phases (i.e., assimilation-fractional crystallization, AFC) during reactive porous flow (Boulanger et al., 2020; Gao et al., 2007; Lissenberg & MacLeod, 2016; Sanfilippo et al., 2020; Zhang et al., 2020). Yet, we have shown that enrichments in Ti as those observed at the rims of analyzed clinopyroxenes cannot be reproduced by simple magmatic differentiation (i.e., fractional crystallization; Figure 9). These Ti enrichments were recently reproduced experimentally after reactive percolation of a primitive MORB in a troctolitic crystal-matrix (Yang et al., 2019). Likewise, the zoning of coarse-grained minerals in the studied olivine gabbros possibly formed after a process of mineral-melt interactions. The peculiar geochemical zoning have been successfully reproduced using the AFC equations proposed by DePaolo (1981) (e.g., Boulanger et al., 2020; Lissenberg & MacLeod, 2016; Lissenberg et al., 2013; Sanfilippo et al., 2015, 2020; Zhang et al., 2020). We thus also performed AFC modeling to test whether a process of reactive crystallization is able to reproduce the ubiquitous over-enrichments in the most incompatible trace elements (i.e., LREE and Zr) observed in the studied olivine gabbros.

The occurrence of large poikilitic clinopyroxene suggests that the percolated matrix was a crystal mush with more than ∼30 vol% occupied by melt between the crystal framework (e.g., Coogan, Saunders, et al., 2000). Because no evidence of dissolution was observed at clinopyroxene grain boundaries, we assume that

clinopyroxene was minor or nearly absent in the initial mush; on the other hand, olivine and plagioclase show resorbed grain boundaries. We thus posit that the crystal mush was mainly composed of olivine (ol_1) + plagioclase (pl_1) and minor clinopyroxene; during the process of melt reactive porous flow, the crystal matrix was partially dissolved and olivine (ol_2) + plagioclase (pl_2) + clinopyroxene (cpx_2) crystallized. Mineral modal compositions of the starting ol_1 + pl_1 crystal mush were determined using MELTS (Ghiorso & Sack, 1995) after 20% of fractional crystallization of a primitive N-MORB from the studied area (Mg# ~62; Coogan et al., 2004). This threshold of melt fractionation was chosen to reproduce a troctolitic matrix containing <5 vol% of clinopyroxene. These computed mineral modes were used to calculate the trace element compositions of the assimilated crystals (ol_1 + pl_1); the latter were determined using the common equation of fractional crystallization after 20% of melt fractionation (ol_1 and pl_1 in equilibrium with $C_{20\%F} = C_0 \times (F^{(Gk-1)})$, where C_0 is the composition of the initial melt, that is, the primitive N-MORB with Yb_N ~15.6; F is the melt fraction; Gk is the global partition coefficient of a given element, determined using the partition coefficients calculated from our mineral compositions using models by C. Sun & Liang, 2014 and C. Sun et al., 2017). The composition of the migrating melt was estimated from the composition of cores of coarse-grained clinopyroxene. Major and trace element compositions of coarse-grained crystal cores are in equilibrium with a N-MORB compositionally similar to the primitive end-members among MORBs from the SWIR (Mg# ~62 mol%; Coogan et al., 2004). The calculated melt (in equilibrium with average core of coarse-grained clinopyroxene) has on average Mg# ~62 mol% and low trace element contents (Yb_N ~17.3; Figure S7). Conversely, rims of coarse-grained clinopyroxene and unzoned fine-grained crystals crystallized from a more evolved melt that, calculated in equilibrium with an average of the fine-grained crystals, has Mg# ~53 mol% and higher trace element contents (average evolved MORB from the SWIR: Yb_N = 25.2; Coogan et al., 2004; Figure S7).

The mineral-melt interaction process described above was modeled assuming the following reaction (AFC-1):

$$0.4ol_1 + 0.6pl_1 + melt_1 = 0.1ol_2 + 0.6pl_2 + 0.3cpx_2 + melt_2$$

where ol_1 (olivine) and pl_1 (plagioclase) constitute the pre-existing crystal matrix (Ma -assimilated mass), $melt_1$ is the migrating melt before reactive crystallization, and ol_2 + pl_2 + cpx_2 (clinopyroxene) are the minerals in equilibrium with the reacted and modified $melt_2$ and constituting the olivine gabbro (Mc—crystallized mass). The mineral modes of the products are representative of the modal compositions of the studied olivine gabbros.

The results of the AFC-1 modeling are reported in Figures 10a and 10b in terms of Yb_N versus Zr_N/Nd_N in clinopyroxene and Sm_N versus Ce_N/Sm_N in plagioclase. Computed AFC-1 trends (Figures 10a and 10b) show the compositions of clinopyroxene and plagioclase in equilibrium with the modified melt during the reactive process ($melt_2$) at progressively decreasing melt mass (F = 0.95–0.05). We set five different Ma/Mc (Ma/Mc = 0.6–0.8) representing different extents of the reactive process. These AFC-1 models succeed in reproducing most of the increase in REE of clinopyroxene and plagioclase (i.e., Yb and Sm, respectively) in olivine gabbros from Hole U1473A. They simulate the lower interval of trace element fractionations, which increase progressively during the reaction and characterize a portion of analyzed fine-grained minerals. Note, however, that our AFC-1 fails to reproduce the most enriched Zr concentrations at rims of coarse-grained clinopyroxene and some fine-grained clinopyroxenes. In the following, we hypothesize a further step of the AFC process to explain the most extreme trace element enrichments.

The strong trace element fractionations observed at rims of coarse-grained and in some fine-grained clinopyroxene (i.e., not explained by AFC-1; Figure 10a) are coupled with constant Ni at increasing REE (Figure 11), thus suggesting that Ni does not vary in the parental melt as crystallization proceeds. This contrasts with the composition of cores of coarse-grained crystals that show decreasing Ni during mineral-melt interactions and progressive crystallization (i.e., at increasing REE; Figure 11). Because Ni partitioning is significantly higher in olivine than in clinopyroxene ($^{ol/melt}Kd_{Ni} \approx 10$ and $^{cpx/melt}Kd_{Ni} \approx 3.8$; Le Roux et al., 2011), variations of Ni contents in clinopyroxene can be used to trace the crystallization of olivine (see also Sanfilippo et al., 2015). Concomitant crystallization of olivine and clinopyroxene leads to decreasing Ni in the parental melts as magmatic crystallization proceeds (Figure 11). When olivine crystallization ceases, Ni becomes only weakly compatible to incompatible, as it is governed by the crystallization of
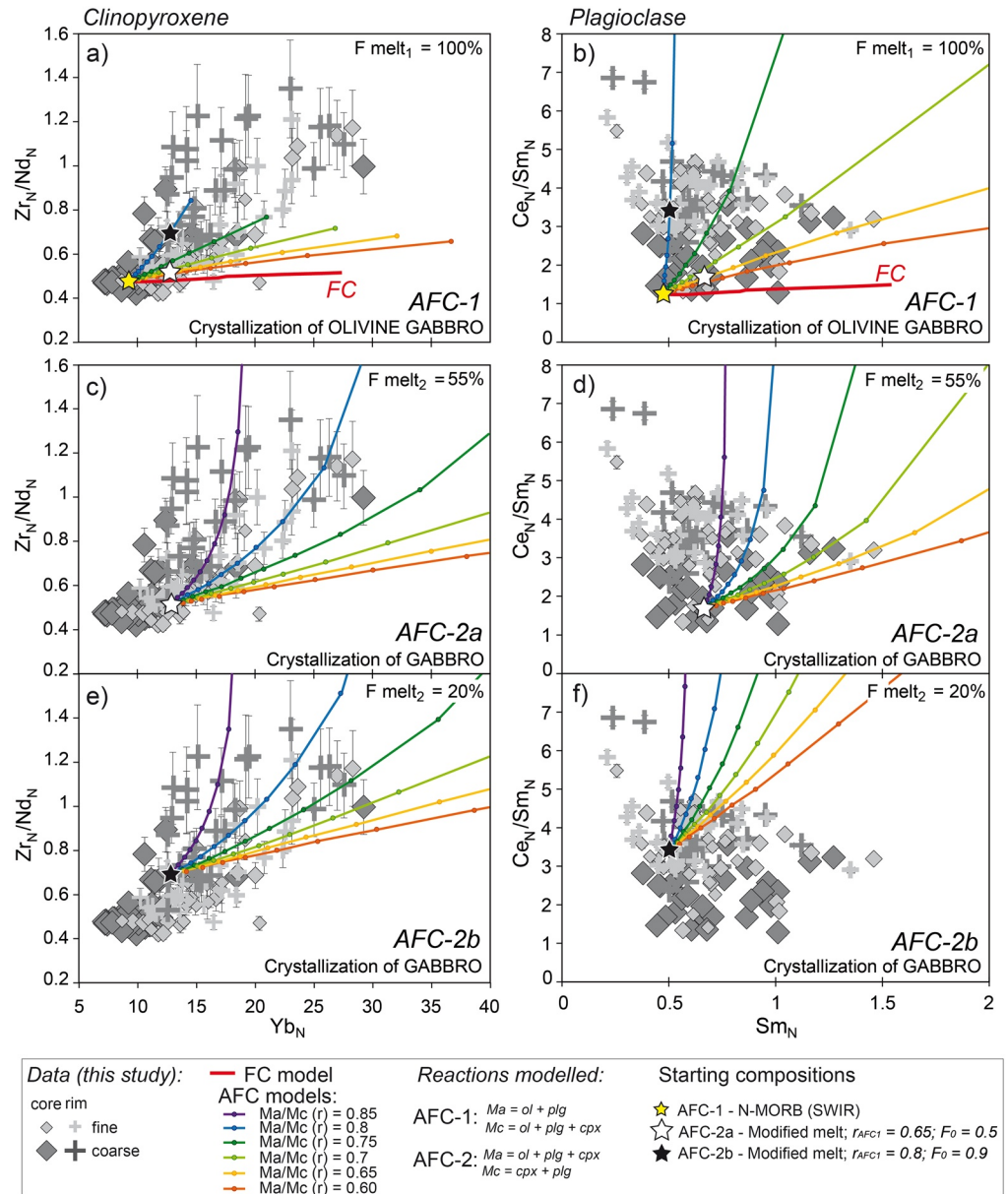
Figure 10. Variation of Zr_N/Nd_N ratio versus Yb_N in clinopyroxene (a, c, e) and Ce_N/Sm_N ratio versus Sm_N in plagioclase (b, d, f) of coarse- (dark gray) and fine-grained (light gray) olivine gabbro from this study. Symbols are as in Figures 5, 6, and 8. Data are compared to clinopyroxene and plagioclase composition computed by AFC models (De Paolo, 1981) at decreasing melt mass and using different Ma/Mc ratios. Partition coefficients were calculated at 1100 °C from mineral compositions measured in this study using the lattice-strain model from C. Sun and Liang (2014) for olivine and clinopyroxene, and C. Sun et al. (2017) for plagioclase. (a and b) Results of AFC-1 models that reproduce olivine + plagioclase assimilation and crystallization of olivine gabbro; first step of the model is computed at $F = 1$ (100% melt mass). The initial melt composition ($melt_1$; yellow star) is equal to the melt computed in equilibrium with the average REE composition of clinopyroxene cores in the more primitive U1473A coarse-grained olivine gabbros. Note that this model does not explain the most over-enrichments in Zr in clinopyroxene. (c and f) Results of AFC-2 models that reproduce assimilation of olivine gabbro from AFC-1 models and crystallization of gabbro. The initial melt and mineral compositions ($melt_2$) are: (c and d) output of AFC-1 run at Ma/Mc = 0.65 after $F = 0.55$ (white star; AFC-2a), first step of AFC-2a model is assumed to correspond to 55% melt mass; (e and f) output of AFC-1 run at Ma/Mc = 0.8 after $F = 0.20$ (blue star; AFC-2b), first step of AFC-2b model is assumed to correspond to 20% melt mass.
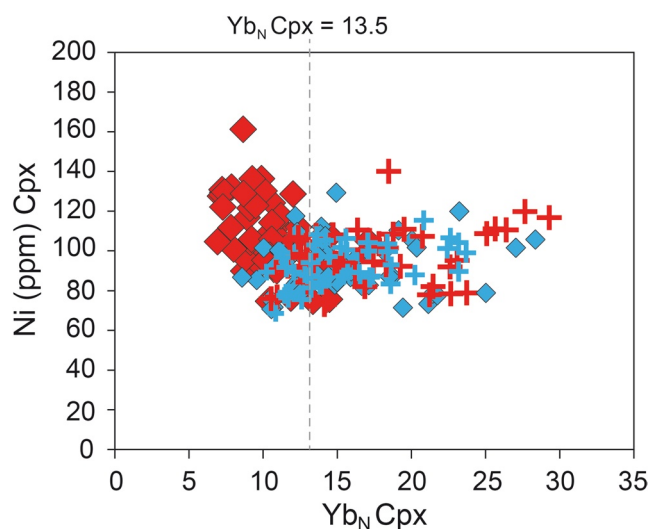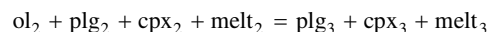
Figure 11. Ni (ppm) versus Yb_N in clinopyroxene. At $Yb_N < \sim13.5$ Ni decrease at increasing Yb_N; at $> \sim13.5$ Ni is nearly constant at increasing Yb_N. Symbols are as in Figures 5 and 6.

plagioclase and clinopyroxene only. Furthermore, experimental studies and thermodynamic evaluations suggest that during melt crystallization and AFC processes, the melt residual from interactions may differentiate following a liquid-line of descent different from that expected by a fractional crystallization process (Basch et al., 2019; M. L. Collier & Kelemen, 2010; Kvassnes & Grove, 2008). Here, we propose that at temperatures ~1050 °C (roughly corresponding to the rims of coarse-grained minerals and to the fine-grained intervals) the melt is no longer saturated in olivine and the crystallizing assemblage is mainly constituted by plagioclase and clinopyroxene (e.g., Feig et al., 2006; Husen et al., 2016). This is demonstrated by the constant Ni contents in the rims of the coarse-grained clinopyroxene as well as in the fine-grained counterparts, which likely crystallized from a residual melt undersaturated in olivine. To test this hypothesis, we performed AFC models to reproduce the geochemical evolution of clinopyroxene and plagioclase during the reaction (AFC-2):

$$ol_2 + plg_2 + cpx_2 + melt_2 = plg_3 + cpx_3 + melt_3$$

where $ol_2 + plg_2 + cpx_2$ constitute the olivine gabbro formed during AFC-1, $plg_3 + cpx_3$ are crystal rims of plagioclase and clinopyroxene, respectively, precipitated from the reacted $melt_3$. We considered the variation in Ni versus Yb_N contents in clinopyroxene to constrain the change in olivine saturation in the melt, and thus to pinpoint the melt composition at which olivine ceased to crystallize. At increasing Yb_N, Ni in clinopyroxene decreases until $Yb_N \sim13.5$, after which it remains relatively constant (Figure 11). The melt in equilibrium with this clinopyroxene has $Yb_N = 23.5$–23.8. We selected this melt composition and the corresponding bulk-rock composition from the output of AFC-1. Two starting compositions were chosen along trends of AFC-1 models run at two distinct Ma/Mc ratios (Figures 10c–10f), by selecting $melt_2$ with $Yb_N \sim 23.5$–23.8:

(i) *AFC-2a* uses bulk rock and melt compositions from AFC-1 run with Ma/Mc = 0.65; $melt_2$ with $Yb_N = 23.5$–23.8 was reproduced after 45% crystallization of N-MORB during AFC-1
(ii) *AFC-2b* uses bulk rock and melt compositions from AFC-1 run with Ma/Mc = 0.8; $melt_2$ with $Yb_N = 23.5$–23.8 was reproduced after 80% crystallization of N-MORB during AFC-1.

The results of the AFC-2 models are reported in Figures 10c–10f. The compositions of plagioclase and clinopyroxene rims are successfully reproduced by AFC-2 at a relatively high Ma/Mc (up to Ma/Mc = 0.85) and considering less than 80% crystallized melt mass. The deepening of the Eu negative anomaly in clinopyroxene from the crystal cores to the rims further indicate the decrease in melt mass during the late stages of the reactive process. Thus, such evolved compositions record the closure of the system and final melt crystallization, which likely occurred at decreasing temperature and porosity of the crystal mush.

We would like to stress that mineral trace element compositions across single grain-size contacts generally lay along the same reaction curve corresponding to a given Ma/Mc of the AFC-1 models (Figure S8). Ma and Mc are function of the rate of assimilation and crystallization, respectively (DePaolo, 1981). The AFC process is thus strongly dependent upon the disequilibrium between the melt and the crystals, which controls the rate of assimilation, and the conditions favoring melt crystallization (i.e., controlling the rate of crystallization). Assuming a constant rate of crystallization, for instance governed by a constant heat removal from the lower oceanic crust (e.g., Coogan et al., 2007), the variable Ma/Mc in the studied olivine gabbros could be related to local variations in melt-mineral chemical disequilibrium. It is possible that locally different melt composition or variations in mineral compositions throughout the crystal mush could enhance or reduce the rate of assimilation.

In conclusion, we here demonstrated that olivine gabbros from IODP Hole U1473A form during two dominant magmatic processes; they involve early crystallization of a gabbroic matrix in a crystal mush, and subsequent mineral-melt reactions driven by melt reactive porous flow.

7.2. Origin of Coarse- Versus Fine-Grained Crystals

We have shown that the studied samples display variations in grain size and have relatively homogeneous mineral modal compositions. The higher crystal density per volume within the fine-grained olivine gabbros compared to the coarse-grained intervals (Figure 3), suggests that nucleation was more efficient during crystallization of the fine-grained crystals. Conversely, crystal growth was the dominant crystallization mechanism during formation of coarse-grained minerals (see Mollo & Hammer, 2017, and references therein). Crystals nucleation and growth are strongly controlled by the difference between liquidus temperature (T_L) and effective temperature of the crystallizing melt (i.e., temperature of the system, T_S), namely the degree of undercooling (e.g., Barbey et al., 2019; Donaldson, 1976; Dowty, 1980; Faure et al., 2003; Kirkpatrick et al., 1976; Martel, 2012; Mollo & Hammer, 2017; Mourey & Shea, 2019; O'Driscoll et al., 2007; Shea et al., 2019). When T_S is close to T_L (i.e., low degrees of undercooling), and for example, when a primitive MORB crystallizes in situ in a rather hot system (∼1200 °C), crystal growth predominates. At rather constant T_L, the undercooling can only increase with the decrease of T_S (see Mollo & Hammer, 2017, and references therein). When T_S starts to decrease (e.g., injection in a relatively cool host rock), and therefore at slightly higher degrees of undercooling, new nuclei start to form and crystallization is dominated by nucleation (Lofgren, 1980). Significant and abrupt perturbations in T_L (e.g., Barbey et al., 2019; Basch et al., 2019; Donaldson, 1977; Hammer & Rutherford, 2002; O'Driscoll et al., 2007; Welsch et al., 2013) can also markedly change the degree of undercooling and leads to disequilibrium growth textures (e.g., Donaldson, 1974; Faure et al., 2007), even at small degrees of undercooling (25°–40°; Shea et al., 2019).

At the Atlantis Bank OCC, we showed that a progressive chemical evolution is recorded from the cores of coarse-grained crystals to their respective rims, the latter sharing the same compositions with the fine-grained minerals; therefore, T_L and T_S are progressively modified upon magmatic differentiation with no abrupt change in both T_L and T_S. Accordingly, the fine-grained intervals are characterized by granular textures of mostly polyhedral crystals (Donaldson, 1974; Faure et al., 2007).

The progressive chemical evolution recorded in coarse-grained minerals resulted from reactive porous flow (see Section 7.1.2). Thermal models indicate that decrease in T_S is expected to accompany a process of chemical equilibration of the melt with the mineral matrix during the process of reactive melt migration in crystal mushes (Solano et al., 2014). This idea is sustained by Sanfilippo et al. (2020) who documented thermal equilibration toward lower T during a process of reactive migration into a melt-rich channel crosscutting an olivine gabbro from Hole U1473A. Following these findings, we suggest that the formation of coarse-grained intervals is thereby characterized by a progressive decrease in T_S, associated with a progressive decrease in T_L due to the change in melt composition during reactive porous flow. This hampered the development of an undercooling, and crystal growth dominated.

The equilibrium temperatures recorded in cores of coarse-grained mineral phases (∼1150 °C; Figure 8a) are ∼100 °C higher than those measured in fine-grained intervals (∼1050 °C; Figure 8a). Rim-rim equilibrium temperatures both in coarse- and fine-grained intervals are comparable to the fine-grained core-core equilibrium temperatures (Figure 8b). This is consistent with the similar compositions of rims of coarse-grained minerals and unzoned fine-grained minerals, thereby indicating that they crystallized from melts having the same composition and T_L. Despite these chemical similarities, textural evidence, that is, growth of rim of coarse-grained crystals versus nucleation of fine-grained minerals, indicate a change in crystallization mechanism due to the presence or absence of pre-existing nuclei. While coarse-grained minerals continuously grew at decreasing T_L and T_S, the same evolved melt was collected in melt-rich intervals with no pre-existing nuclei, thus possibly preventing crystal growth. This likely led to a delay in nucleation in those melt-rich domains (e.g., Koepke et al., 2011; Mollo & Hammer, 2017 and references therein) that allowed the T_L to remain constant during the progressive cooling of the system (i.e., decrease in T_S). This generated significant undercooling in those areas, and in turn enhanced crystals nucleation rate, leading to the formation of the fine-grained olivine-gabbro.

To summarize, we infer that coarse-grained intervals formed during melt reactive percolation in a crystal mush at temperatures T_S close to the T_L of the melts (i.e., low undercooling). These conditions favored the growth of pre-existing minerals associated with low nucleation rates (e.g., Martel, 2012). Upon cooling, and likely due to melt segregation, a delay in nucleation created a significant undercooling, in turn resulting in

the crystallization of melt-rich intervals dominated by crystal nucleation. Simultaneously, in the coarse-grained intervals, the interstitial melts, compositionally similar to fine-grained minerals, precipitated at the crystal rims due to the presence of pre-existing nuclei, and have the most evolved compositions. We emphasize that the equilibrium temperatures recorded in the fine-grained intervals likely do not represent the temperature of melt segregation, but rather are minimum estimates of the crystallization temperature of the adcumulate fine-grained olivine gabbros (i.e., when olivine, plagioclase and clinopyroxene crystallized simultaneously). Nonetheless, the 100 °C difference between coarse- and fine-grained intervals represents the primary difference in crystallization temperature.

7.3. Reconstructing the Temporal Evolution of Grain-Size Variations

7.3.1. Two Distinct Grain-Size Contacts

Minor compositional variations are observed between coarse- and fine-grained minerals across planar contacts defining an igneous layering in Hole U1473A (Boulanger, 2020; Figure 12). Conversely, minerals across irregular contacts from this study display different within-sample chemical heterogeneity. In particular, *Type 1* and *Type 2* irregular contacts can be distinguished by distinct variations in mineral compositions across the contacts (Figure 12). Based on structural relationships and mineral geochemical compositions, we identified the two types of contacts as follows.

Sharp grain-size contacts show preserved thick intervals of coarse-grained olivine gabbro (*Type 1*; Figure 3a). The mineral compositional variations between coarse- and fine-grained intervals are notable. For any given coarse-grained domain, rims of plagioclase and clinopyroxene are systematically more evolved than relative crystal cores. The crystal rims and the nearly unzoned fine-grained crystals show similar compositions (Figure 12). This is for instance shown by the covariations in increasing Ti with decreasing Mg# in clinopyroxene (Figure 9a), and by the progressive over-enrichments in highly incompatible elements (Ce_N/Sm_N in plagioclase; Ce_N/Y_N and Zr_N/Nd_N in clinopyroxene).

Diffuse grain-size contacts display coarse-grained olivine gabbro occurring in few centimeter-thick levels, locally embayed within the fine-grained intervals (*Type 2*; Figure 3c). Overall, they display homogeneous compositions of coarse- to fine-grained minerals (Figures 9b and 12), although REE contents of fine-grained clinopyroxene cores are slightly higher than the coarse-grained counterparts (Figure 7c, Figure S2e). Over-enrichments in the most incompatible elements are preferentially observed at rims of coarse-grained clinopyroxene.

Selected olivine gabbros not only record melt migration and melt chemical evolution in a reactive porous flow process (see Section 7.1.2), but also document for the first time the segregation of melts modified by this reactive process (see Section 7.2). Variations in mineral chemical compositions are systematic between coarse and fine-grained crystals across *sharp irregular* contacts (Figure 12), whereas *diffuse irregular* contacts show rather homogeneous mineral chemistry (Figure 12), with the clinopyroxene exception recording incompatible element differences (Figures 7c and 7d, Figures S2e and S2f). We infer that distinct mechanisms of reactive crystallization control mineral compositions across the two types of irregular contacts in olivine gabbros. Based on numerical simulations of melt flow in crystal mushes, Hersum et al. (2005) proposed that melt flow is markedly dependent on melt fraction: melt migration is diffuse between crystals at high melt fractions, and becomes focused with decreasing melt fraction. At *sharp* contacts, fine-grained olivine gabbros are decimeter-thick discrete intervals indicating focused melt migration, as similarly described in the Oman Ophiolite (e.g., Korenaga & Kelemen, 1997, 1998). This testifies melt migration at relatively low melt fractions in the selected fine-grained intervals presenting *sharp* contacts. In contrast, the ~meter-thick fine-grained intervals characterized by *diffuse* contacts possibly document pervasive melt migration at high melt/rock ratio (M. L. Collier & Kelemen, 2010; Saper & Liang, 2014; Van den Bleeken et al., 2011).

Throughout Hole U1473A, the difference in melt fraction between *sharp* and *diffuse* contacts might be related to the heterogeneous distribution of crystals in the crystal mush, in turn leading to heterogeneous crystal/melt ratios. This heterogeneity may be enhanced by local variations in the strength of compaction of the crystal pile. In this scenario, higher crystal/melt ratios (i.e., lower melt fraction) allow melts to migrate at higher flow rates increasing the degree of channelization (Bergantz et al., 2015). The reacted melts
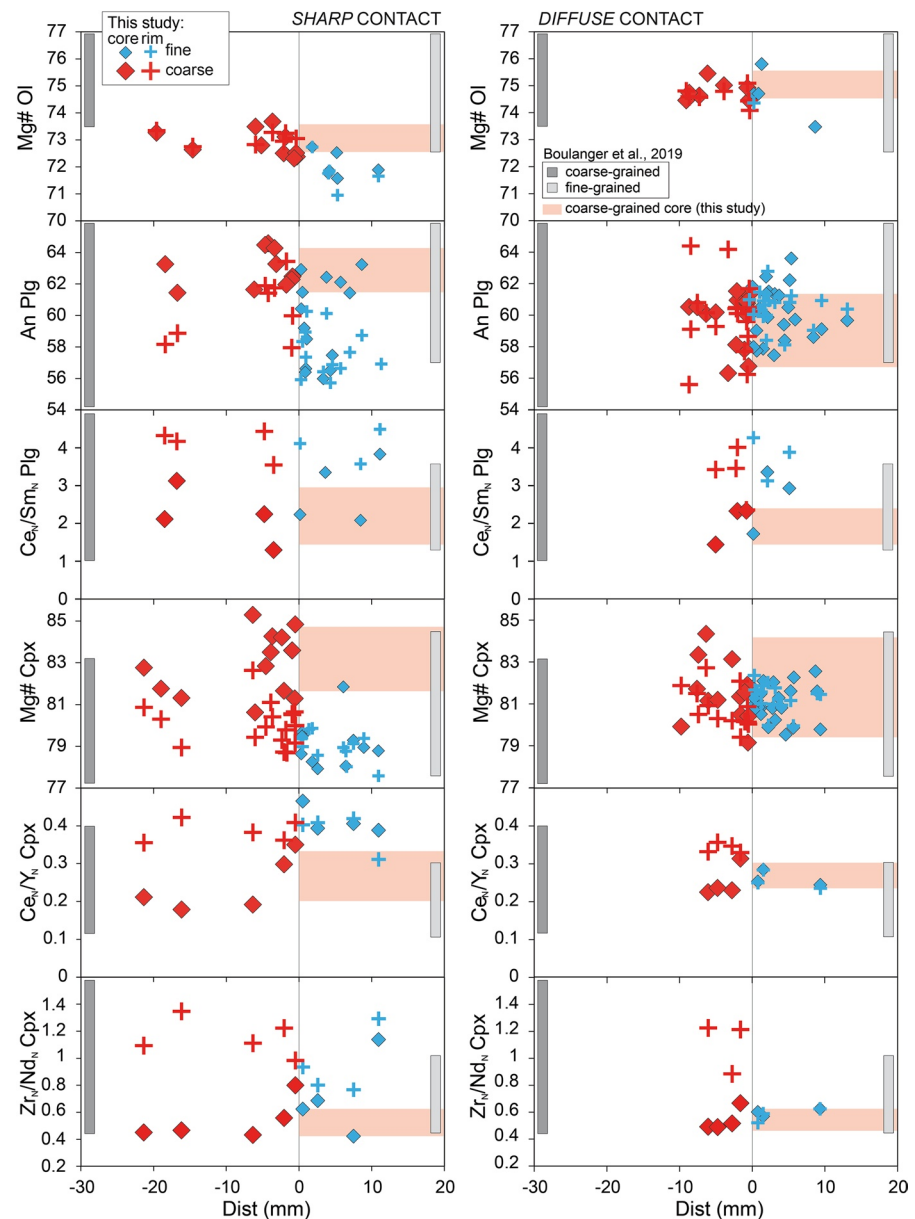
Figure 12. Profiles of mineral (Ol = olivine, Plg = plagioclase, Cpx = clinopyroxene) chemical compositions across grain-size contacts where coarse-grained crystals are plotted on the left and fine-grained on the right of the contact (placed at 0). Two representative samples are selected: one for sharp contacts (left column; sample 360-U1473A-73R-1W, 41–47 cm) and one for diffuse contacts (right column; sample 360-U1473A-68R-5W, 64–70 cm). Red boxes are compositions of cores of coarse-grained crystals. Gray bars indicate compositional variability of coarse- (dark) and fine-grained (light) minerals in layering within olivine gabbro from the same Hole U1473A (Boulanger, 2020).

migrate by focused flow, and as temperature decreases, they segregate in discrete intervals to form the fine-grained olivine gabbro. Coarse-grained intervals are preserved, and minerals retain their primary chemical composition (i.e., composition of crystal cores) as observed across *sharp* contacts in this study. Conversely, melt migration occurs interstitially between coarse-grained crystals in zones with originally lower crystal/melt ratios (i.e., high melt fraction). There, high fractions of reacted melt completely reset the chemical composition of enclosed coarse-grained phases and crystallize the fine-grained olivine gabbro, thus originating the described *diffuse* contacts.

7.3.2. From Melt Migration to Melt Segregation Throughout the Lower Oceanic Crust

Geophysical data indicate that at early stages of formation, the magmatic bodies building the oceanic crust likely contain melt with sparse crystals (Singh et al., 2006; Sinha et al., 1997). When the interstitial melts are mobilized, the buoyant melt migration and related melt-mineral interactions lead to upward chemical differentiation trends recorded in the crystallized phases (see Boulanger et al., 2020; Lissenberg et al., 2019, and references therein). Textures and mineral geochemical compositions coupled with AFC models indicate that also in Hole U1473A interstitial melts were mobilized and reacted with the pre-existing crystal mush (Figure 13).

The composition of cores of coarse-grained minerals, partly reproduced by magmatic crystallization, together with reactive textures of olivine and plagioclase, indicate that they constitute the early crystallized phases in the crystal mush ($ol_1 + pl_1 \pm cpx_1$; Figure 13a). Due to faster diffusion in olivine compared to plagioclase (e.g., Cherniak, 2003, 2010; Dohmen et al., 2007; Van Orman et al., 2014), olivine in the crystal mush is rapidly re-equilibrated with the reactive migrating melts by element diffusion, whereas cores of coarse-grained plagioclase typically preserve their primary composition. In interval 570–750 mbsf of IODP Hole U1473A, downhole An variations in cores of coarse-grained plagioclase are limited (58–62 mol%), with no systematic evolution trend (Figure 14a). We infer that these compositions represent the primary composition of plagioclase prior to melt-mineral interactions and indicate a relatively homogeneous composition of the pristine crystal mush (Figures 13a and 14b: Step 1). In contrast, within the same depth interval, bulk-rock Mg# (mainly defined by olivine gabbros; Figures 2 and 14c), and Mg# and Cr contents in cores of coarse-grained clinopyroxene decrease upwards (Figures 14c and 14d). Because clinopyroxene is considered in this study as a product of the AFC process, we relate this upward chemical evolution to the differentiation of melts migrating to shallower depths (see also Lissenberg et al., 2019; Figure 14b: Step 2) during reactive porous flow (Figure 13b). Based on the thickness of the interval in which clinopyroxene and bulk compositions evolve upward, melt migration and reaction most likely occurred within an individual magmatic unit of ∼200 m thickness (Figures 14c and 14d); such a thickness is also consistent with the reservoir size identified at ODP Hole 735B drilled in Atlantis Bank (Boulanger et al., 2020).

The rims of coarse-grained crystals and the unzoned fine-grained minerals crystallized from genetically related parental melts (see Section 7.1.2). The latter correspond to melts modified by the mineral-melt interactions in the coarse-grained crystal mush. The formation of fine-grained olivine gabbros, involving enhanced crystal nucleation and hampered crystal growth, required the collection and accumulation of residual melts within discrete intervals where crystal nuclei were nearly absent (Figures 13b and 13c). This promoted a delay in nucleation, thereby increasing the degree of undercooling (see Section 7.2). The melt-rich intervals likely represented zones of high porosity within the crystal mush. When the system cooled, these residual melts remained segregated and crystallization was progressively dominated by nucleation (i.e., at enhanced undercooling), thereby leading to the formation of the adcumulate fine-grained olivine gabbros (Figure 13c).

The ubiquitous textural and geochemical evidence of melt-mush interactions (mainly in coarse-grained intervals) and the occurrence of the fine-grained olivine gabbros throughout Hole U1473A indicate that reactive melt migration affected large portions of lower crust crystal mush, and that residual melts were collected and ultimately segregated at all depths in the lower oceanic crust at the Atlantis Bank OCC (Figure 14e: Step 3). This implies that the initial stages of melt migration through the coarse-grained crystal-mush occurred interstitially between pre-existing crystals, and produced the geochemical evolution trends within a single chemical unit by pervasive melt transport (Figures 14b–14d: Step 2). The melts residual from the reactive processes accumulate in discrete zones where melt transport was driven by two main mechanisms. *Diffuse* contacts result from pervasive melt migration, while *sharp* contacts record focused melt migration. Both pervasive and focused melt transport occurred locally, at the scale of single fine-grained intervals (less than a meter) and governed the composition of microgabbros. The equal and homogeneous distribution with depth of the two types of contacts indicate that no predominant mechanism drove local melt transport. The local character of melt collection implies that the accumulated melts originated in the associated coarse-grained olivine gabbros as evidenced by systematically more evolved compositions of microgabbros with respect to their coarse-grained counterpart; therefore, the primary chemical trend produced by early porous flow in the coarse-grained crystal mush (Figures 14a–14c: Step 2) was not affected by the diffuse and
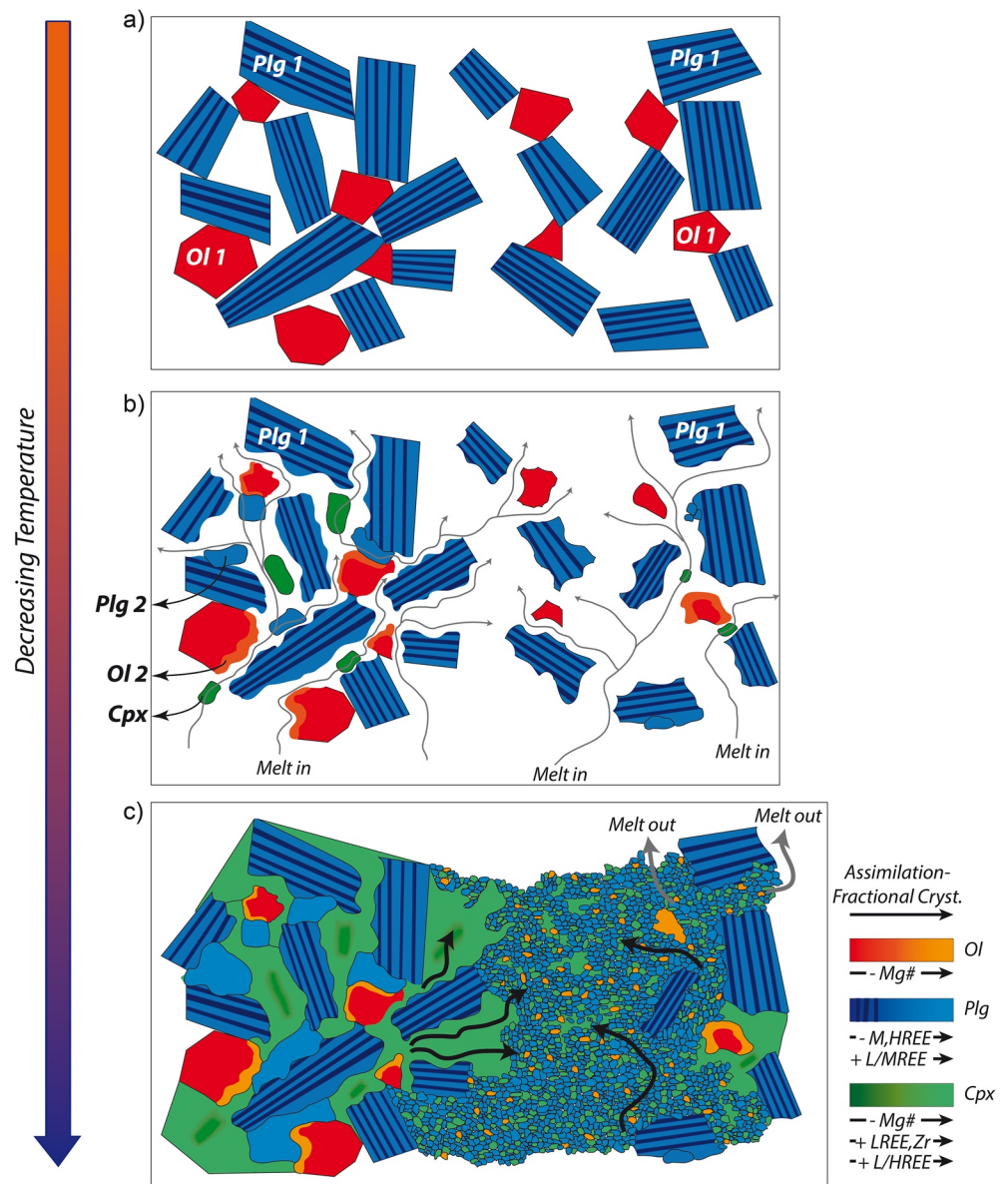
Figure 13. Schematic reconstruction of the microstructure and chemical evolution from crystal mush to formation of grain-size variations in the studied olivine gabbro. The processes recorded can be summarized as follows. (a) Heterogeneously distributed olivine + plagioclase crystals form after crystallization in situ (up to 20%–30% of melt fractionation) of primitive melts in a crystal mush. (b) Melts within the crystal mush (possibly residual from former minerals crystallization) begin to migrate through the permeable olivine + plagioclase (±clinopyroxene?) framework and, being in disequilibrium with the more primitive compositions of pre-existing minerals, partially dissolve olivine$_1$ and plagioclase$_1$ and concomitantly crystallize olivine$_2$, plagioclase$_2$, and clinopyroxene$_2$; crystals preferentially grow and coarse-grained intervals are formed at temperatures of ~1150 °C. Note that only plagioclase and olivine display resorbed grain boundaries, while clinopyroxene does not show textural evidences of dissolution. It is possible that few crystals of clinopyroxene$_1$ also formed the pre-existing crystal mush; some crystal cores could represent former clinopyroxene, but we have no certain and clear evidence at this point. (c) The reactive melt migration proceeds at decreasing T_L and T_S. Melts residual from interaction both crystallize at the rims of pre-existing coarse-grained minerals and are pervasively collected in high porosity zones. In these zones, the delay in nucleation produces an increase in undercooling at decreasing T_S that ultimately results in high nucleation rates; new nuclei preferentially form, and the segregated residual melts crystallize to form the fine-grained olivine gabbros at temperatures of ~1050 °C.
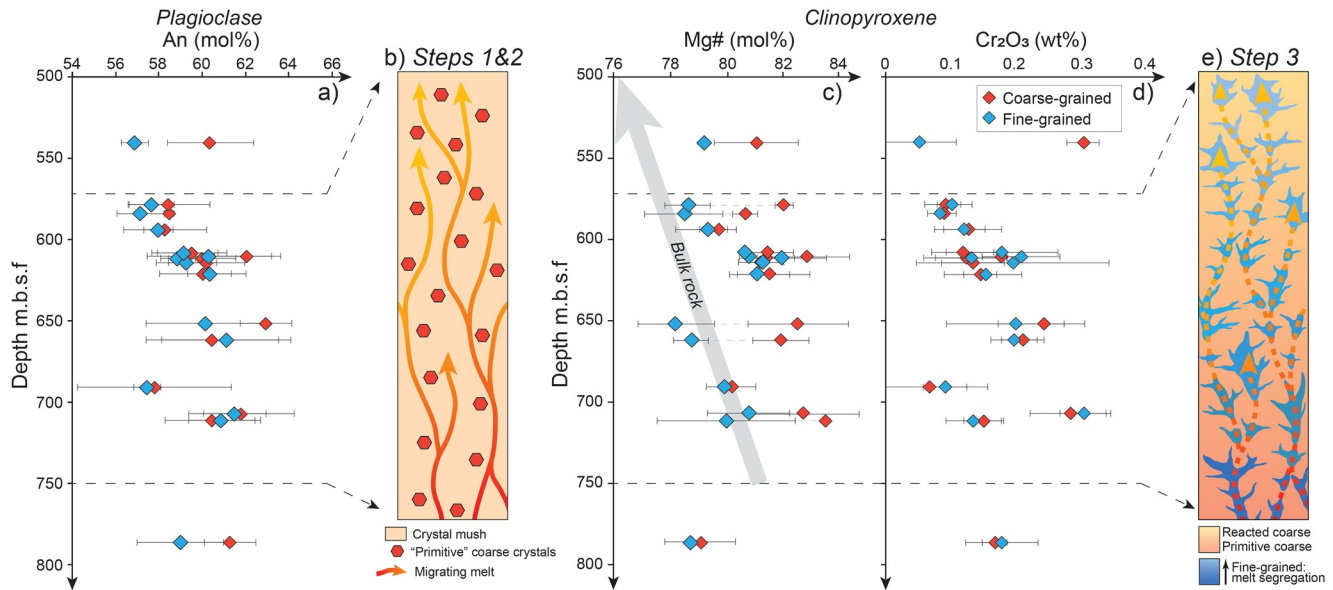
Figure 14. Downhole An contents in plagioclase cores (a) and Mg# (c) and Cr_2O_3 (wt%; d) in clinopyroxene cores in olivine gabbro from this study, in the depth interval 500–810 mbsf. Data are averages of coarse- and fine-grained minerals from each studied sample; the gray arrow in Mg# plot (c) shows the upward chemical trend of bulk-rock compositions of olivine gabbro from Hole U1473A in the studied depth interval (MacLeod et al., 2017). Rather homogeneous compositions of coarse-grained plagioclase possibly represent components of the former crystal mush (b; Step 1) percolated by reactive melts (b; Step 2). Upward evolution of bulk and clinopyroxene compositions likely testifies the progressive differentiation of migrating melts. Such melts are ultimately segregated at all depths and form the fine-grained olivine gabbro.

focused melt transport and accumulation (Figure 14e: Step 3). Because bulk-rock analyses of fine-grained intervals show a cumulitic character (L. France, unpublished data), it is plausible that accumulated melts were further extracted from the melt-rich pockets (microgabbros), chemically contributing to MORBs.

8. Concluding Remarks

Textures and mineral geochemical compositions coupled with AFC models are consistent with formation of U1473A olivine gabbros from ubiquitous processes of reactive porous flow of melts through a pre-existing crystal mush, which concomitantly led to upward chemical differentiation of these migrating melts. We document that the complex history of crystal mush emplacement and mineral-melt interactions at the Atlantis Bank OCC are mainly recorded in coarse-grained intervals. Fine-grained olivine gabbros testify collection and segregation of the melts residual from the reactive process, governed by cooling of the lower oceanic crust (from ∼1150°C to ∼1050 °C). The cooling could result from two processes. The first implies initiation of the detachment fault responsible for the exhumation of the lower oceanic crust at OCCs; thereby, uplifting of gabbroic sequences has been reported as efficient mechanism of heat removal (e.g., Coogan et al., 2007; Ferrando et al., 2020) At the Atlantis Bank OCC, the average cooling rates of ∼0.005 °C/yr (Coogan et al., 2007; John et al., 2004) could be responsible for the decrease in the temperature of the system (T_S). It is plausible that exhumation was associated with reduced melt income, which further diminished the heat supply to the lower oceanic crust and thus enhanced cooling. The second potential process triggering the cooling of the forming lower oceanic crust is the melt evolution by AFC, which is documented to be endothermic (e.g., Kelemen, 1990; Solano et al., 2014).

Geochemical compositions of erupted MORBs from different locations record melt-mineral interactions occurring in the lower oceanic crust (e.g., Boulanger et al., 2020; Lissenberg & Dick, 2008; Lissenberg et al., 2013). Our study of grain-size variations throughout IODP Hole U1473A allows identifying for the first time the collection and accumulation of melts residual from the reactive process in high-porosity zones, throughout the lower oceanic crust. Both at *diffuse* and *sharp grain-size* contacts, we propose that these accumulated melts can be at some point extracted from the lower oceanic crust and, therefore, can chemically contribute to the erupted MORBs.

Data Availability Statement

The geochemical data used in this study are included as tables in the supporting information. The data published will be contributed to the Petrological Database (www.earthchem.org/petdb) and available through Ferrando et al. (2021).

References

Abily, B., & Ceuleneer, G. (2013). The dunitic mantle-crust transition zone in the Oman ophiolite: Residue of melt-rock interaction, cumulates from high-MgO melts, or both? *Geology*, *41*, 67–70. https://doi.org/10.1130/G33351.1

Baines, A. G., Cheadle, M. J., John, B. E., & Schwartz, J. J. (2008). The rate of oceanic detachment faulting at Atlantis Bank, SW Indian Ridge. *Earth and Planetary Science Letters*, *273*, 105–114. https://doi.org/10.1016/j.epsl.2008.06.013

Barbey, P., Faure, F., Paquette, J., Pistre, K., Delangle, C., & Gremilliet, J.-P. (2019). Skeletal quartz and dendritic biotite: Witnesses of primary disequilibrium growth textures in an alkali-feldspar granite. *Lithos*, *348–349*, 105202. https://doi.org/10.1016/j.lithos.2019.105202

Basch, V., Rampone, E., Crispini, L., Ferrando, C., Ildefonse, B., & Godard, M. (2018). From mantle peridotites to hybrid troctolites: Textural and chemical evolution during melt-rock interaction history. *Lithos*, *323*, 4–23. https://doi.org/10.1016/j.lithos.2018.02.025

Basch, V., Rampone, E., Crispini, L., Ferrando, C., Ildefonse, B., & Godard, M. (2019). Multi-stage reactive formation of troctolites in Slow-spreading Oceanic Lithosphere (Erro—Tobbio, Italy): A combined field and petrochemical study. *Journal of Petrology*, *60*(5), 873–906. https://doi.org/10.1093/petrology/egz019

Bédard, J. H. (1994). A procedure for calculating the equilibrium distribution of trace elements among the minerals of cumulate rocks, and the concentration of trace elements in the coexisting liquids. *Chemical Geology*, *118*, 143–153. https://doi.org/10.1016/0009-2541(94)90173-2

Bédard, J. H., Hebert, R., Berclaz, A., & Varfalvy, V. (2000). Syntexis and the genesis of lower oceanic crust. In Y. Dilek, E. M. Moores, D. Elthon, & A. Nicolas (Eds.), *Ophiolites and oceanic crust: New insights from field studies and the Ocean Drilling Program* (Vol. *349*, pp. 105–119). Special Paper of the Geological Society of America. https://doi.org/10.1130/0-8137-2349-3.105

Bédard, J. H., Leclerc, F., Harris, L. B., & Goulet, N. (2009). Intra-sill magmatic evolution in the Cummings Complex, Abitibi greenstone belt: Tholeiitic to calc-alkaline magmatism recorded in an Archaean subvolcanic conduit system. *Lithos*, *111*, 47–71. https://doi.org/10.1016/j.lithos.2009.03.013

Bergantz, G. W., Schleicher, J. M., & Burgisser, A. (2015). Open-system dynamics and mixing in magma mushes. *Nature Geoscience*, *8*, 10. https://doi.org/10.1038/ngeo2534

Blackman, D. K., Ildefonse, B., John, B. E., Ohara, Y., Miller, D. J., Abe, N., et al. (2011). Drilling constraints on lithospheric accretion and evolution at Atlantis Massif, Mid-Atlantic Ridge 30°N. *Journal of Geophysical Research*, *116*, 1–25. https://doi.org/10.1029/2010JB007931

Blackman, D. K., Ildefonse, B., John, B. E., Ohara, Y., Miller, D. J., MacLeod, C. J., & the Expedition 304/305 Scientists. (2006). Proceedings of the Integrated Ocean Drilling Program (Vol. *304/305*). College Station, TX: Integrated Ocean Drill Program Manage Int. https://doi.org/10.2204/iodp.sp.304305.2004

Borghini, G., & Rampone, E. (2007). Postcumulus processes in oceanic-type olivine-rich cumulates: The role of trapped melt crystallization versus melt/rock interaction. *Contributions to Mineralogy and Petrology*, *154*, 619–633. https://doi.org/10.1007/s00410-007-0217-5

Boulanger, M. (2020). *The fate of melts within the slow-spreading lower oceanic crust: New insights from Atlantis Bank (Southwest Indian Ridge)* (PhD thesis): Earth Sciences, Université de Lorraine.

Boulanger, M., France, L., Deans, J. R., Ferrando, C., Lissenberg, J., & von der Handt, A. (2020). Magma reservoir formation and evolution at a slow-spreading center (Atlantis Bank, Southwest Indian Ridge). *Frontiers in Earth Sciences*. https://doi.org/10.3389/feart.2020.554598

Canales, J. P., Nedimovic, M. R., Kent, G. M., Carbotte, S. M., & Detrick, R. S. (2009). Seismic reflection images of a near-axis melt sill within the lower crust at the Juan de Fuca ridge. *Nature*, *460*, 89–94. https://doi.org/10.1038/nature08095

Cannat, M., Sauter, D., Mendel, V., Ruellan, E., Okino, K., Escartin, J., et al. (2006). Modes of seafloor generation at a melt-poor ultraslow-spreading ridge. *Geology*, *34*, 605–608. https://doi.org/10.1130/G22486.1

Cashman, K. V., Sparks, R. S. J., & Blundy, J. D. (2017). Vertically extensive and unstable magmatic systems: A unified view of igneous processes. *Science*, *355*, 6331. https://doi.org/10.1126/science.aag3055

Cherniak, D. J. (2003). REE diffusion in feldspar. *Chemical Geology*, *193*, 25–41. https://doi.org/10.1016/S0009-2541(02)00246-2

Cherniak, D. J. (2010). REE diffusion in olivine. *American Mineralogist*, *95*, 362–368. https://doi.org/10.2138/am.2010.3345

Collier, J. S., & Singh, S. C. (1998). A seismic inversion study of the axial magma chamber reflector beneath the East Pacific Rise near 10°N. *Geological Society, London, Special Publications*, *148*, 17–28. https://doi.org/10.1144/GSL.SP.1998.148.01.02

Collier, M. L., & Kelemen, P. B. (2010). The case for reactive crystallization at mid-ocean ridges. *Journal of Petrology*, *51*, 1913–1940. https://doi.org/10.1093/petrology/egq043

Coogan, L. A., Hain, A., Stahl, S., & Chakraborty, S. (2005). Experimental determination of the diffusion coefficient for calcium in olivine between 900°C and 1500°C. *Geochimica et Cosmochimica Acta*, *69*, 3683–3694. https://doi.org/10.1016/j.gca.2005.03.002

Coogan, L. A., Jenkin, G. R. T., & Wilson, R. N. (2007). Contrasting cooling rates in the lower oceanic crust at fast- and slow-spreading ridges revealed by geospeedometry. *Journal of Petrology*, *48*, 2211–2231. https://doi.org/10.1093/petrology/egm057

Coogan, L. A., Kempton, P. D., Saunders, A. D., & Norry, M. J. (2000). Melt aggregation within the crust beneath the Mid-Atlantic Ridge: Evidence from plagioclase and clinopyroxene major and trace element compositions. *Earth and Planetary Science Letters*, *176*, 245–257.

Coogan, L. A., & O'Hara, M. J. (2015). MORB differentiation: In situ crystallization in replenished-tapped magma chambers. *Geochimica et Cosmochimica Acta*, *158*, 147–161. https://doi.org/10.1016/j.gca.2015.03.010

Coogan, L. A., Saunders, A. D., Kempton, P. D., & Norry, M. J. (2000). Evidence from oceanic gabbros for porous melt migration within a crystal mush beneath the Mid-Atlantic Ridge. *Geochemistry, Geophysics, Geosystems*, *1*(9). https://doi.org/10.1029/2000GC000072

Coogan, L. A., Thompson, G. M., MacLeod, C. J., Dick, H. J. B., Edwards, S., Hosford Scheirer, A., & Barry, T. (2004). A combined basalt and peridotite perspective on 14 million years of melt generation at the Atlantis Bank segment of the Southwest Indian Ridge: Evidence for temporal changes in mantle dynamics? *Chemical Geology*, *207*, 13–30. https://doi.org/10.1016/j.chemgeo.2004.01.016

DePaolo, D. J. (1981). Trace element and isotopic effects of combined wallrock assimilation and fractional crystallization. *Earth and Planetary Science Letters*, *53*, 189–202. https://doi.org/10.1016/0012-821X(81)90153-9

Dick, H. J. B., Lin, J., & Schouten, H. (2003). An ultraslow-spreading class of ocean ridge. *Nature*, *426*, 405–412. https://doi.org/10.1038/nature02128

Dick, H. J. B., MacLeod, C. J., Blum, P., Abe, N., Blackman, D. K., Bowles, J. A., et al. (2019). Dynamic accretion beneath a slow-spreading ridge segment: IODP Hole 1473A and the Atlantis Bank Oceanic Core Complex. *Journal of Geophysical Research: Solid Earth*, *124*, 2631–12659. https://doi.org/10.1029/2018JB016858

Dick, H. J. B., Meyer, P. S., Bloomer, S., Kirby, S., Stakes, D., & Mawer, C. (1991). Lithostratigraphic evolution of an in-situ section of oceanic Layer 3. In R. P. Von Herzen, & P. T. Robinson (Eds.), *Proceedings of the Ocean Drill Program, scientific results* (Vol. *118*, pp. 439–538). College Station, TX: Ocean Drill Program. https://doi.org/10.2973/odp.proc.sr.118.128.1991

Dick, H. J. B., Natland, J. H., Alt, J. C., Bach, W., Bideau, D., Gee, J. S., et al. (2000). A long in situ section of the lower ocean crust: Results of ODP Leg 176 drilling at the Southwest Indian Ridge. *Earth and Planetary Science Letters*, *179*, 31–51. https://doi.org/10.1016/S0012-821X(00)00102-3

Dick, H. J. B., Ozawa, K., Meyer, P. S., Niu, Y., Robinson, P. T., Constantin, M., et al. (2002). Primary silicate mineral chemistry of a 1.5-km section of very slow spreading lower ocean crust: ODP Hole 753B, Southwest Indian Ridge. *Proceedings of the Ocean Drilling Program*, *176*, 1–61. https://doi.org/10.2973/odp.proc.sr.176.001.2002

Dick, H. J. B., Schouten, H., Meyer, P. S., Gallo, D. G., Bergh, H., Tyce, R., et al. (1991). Tectonic evolution of the Atlantis II Fracture Zone. In R. P. Von Herzen, & P. T. Robinson (Eds.), *Proceedings of the Ocean Drilling Program, scientific results* (Vol. *118* (pp. 359–398). College Station, TX: Ocean Drill Program. https://doi.org/10.2973/odp.proc.sr.118.156.1991

Dick, H. J. B., Tivey, M. A., & Tucholke, B. E. (2008). Plutonic foundation of a slow-spreading ridge segment: Oceanic core complex at Kane Megamullion, 23°30'N, 45°20'W. *Geochemistry, Geophysics, Geosystems*, *91*(59). https://doi.org/10.1029/2007GC001645

Dohmen, R., Becker, H. W., & Chakraborty, S. (2007). Fe-Mg diffusion in olivine I: Experimental determination between 700 and 1200°C as a function of composition, crystal orientation and oxygen fugacity. *Physics and Chemistry of Minerals*, *34*, 389–407. https://doi.org/10.1007/s00269-007-0157-7

Donaldson, C. H. (1974). Olivine crystal types in harrisitic rocks of the Rhum pluton and in Archean spinifex rocks. *GSA Bulletin*, *85*(11), 1721–1726. https://doi.org/10.1130/0016-7606(1974)85<1721:OCTIHR>2.0.CO;2

Donaldson, C. H. (1976). An experimental investigation of olivine morphology. *Contributions to Mineralogy and Petrology*, *57*, 187–213. https://doi.org/10.1007/BF00405225

Donaldson, C. H. (1977). Laboratory duplication of comb layering in Rhum pluton. *Mineralogical Magazine*, *41*, 323–336. https://doi.org/10.1180/minmag.1977.041.319.03

Dowty, E. (1980). Crystal growth and nucleation theory and the numerical simulation of igneous crystallization. In R. B. Hargraves (Ed.), *Physics of magmatic processes* (pp. 419–486). Princeton University Press. https://doi.org/10.1515/9781400854493.419

Drouin, M., Godard, M., Ildefonse, B., Bruguier, O., & Garrido, C. J. (2009). Geochemical and petrographic evidence for magmatic impregnation in the oceanic lithosphere at Atlantis Massif, Mid-Atlantic Ridge (IODP Hole U1309D, 30°N). *Chemical Geology*, *264*, 71–88. https://doi.org/10.1016/j.chemgeo.2009.02.013

Dunn, R. A., Toomey, D. R., & Solomon, S. C. (2000). Three-dimensional seismic structure and physical properties of the crust and shallow mantle beneath the East Pacific Rise at 9°30'N. *Journal of Geophysical Research*, *105*, 23537–23555. https://doi.org/10.1029/2000JB900210

Elthon, D. (1979). High magnesian liquids as the parental magma for ocean floor basalts. *Nature*, *278*, 514–518. https://doi.org/10.1038/278514a0

Elthon, D., Stewart, M., & Ross, K. (1992). Compositional trends of minerals in oceanic cumulates. *Journal of Geophysical Research*, *97*, 15189–15199. https://doi.org/10.1029/92JB01187

Escartín, J., Smith, D. K., Cann, J., Schouten, H., Langmuir, C. H., & Escrig, S. (2008). Central role of detachment faults in accretion of slow-spreading oceanic lithosphere. *Nature*, *455*, 790–794. https://doi.org/10.1002/2014GC005269

Faak, K., & Gillis, K. M. (2016). Slow cooling of the lowermost oceanic crust at the fast-spreading East Pacific Rise. *Geology*, *44*, 115–118. https://doi.org/10.1130/G37353.1

Faure, F., Schiano, P., Trolliard, G., Nicollet, C., & Soulestin, B. (2007). Textural evolution of polyhedral olivine experiencing rapid cooling rates. *Contributions to Mineralogy and Petrology*, *153*, 405–416. https://doi.org/10.1007/s00410-006-0154-8

Faure, F., Trolliard, G., Nicollet, C., & Montel, J.-M. (2003). A developmental model of olivine morphology as a function of the cooling rate and the degree of undercooling. *Contributions to Mineralogy and Petrology*, *145*, 251–263. https://doi.org/10.1007/s00410-003-0449-y

Feig, S. T., Koepke, J., & Snow, J. E. (2006). Effect of water on tholeiitic basalt phase equilibria: An experimental study under oxidizing conditions. *Contributions to Mineralogy and Petrology*, *152*, 611–638. https://doi.org/10.1007/s00410-006-0123-2

Ferrando, C., France, L., Basch, V., Sanfilippo, A., Tribuzio, R., & Boulanger, M. (2021). *In situ mineral major, minor and trace element concentrations in olivine, plagioclase and clinopyroxene from olivine gabbros recovered in IODP Hole U1473A at the Atlantis Bank OCC (57°E, Southwest Indian Ridge), Version 1.0*: Interdisciplinary Earth Data Alliance (IEDA). https://doi.org/10.26022/IEDA/111818

Ferrando, C., Godard, M., Ildefonse, B., & Rampone, E. (2018). Melt transport and mantle assimilation at Atlantis Massif (IODP Site U1309): Constraints from geochemical modeling. *Lithos*, *323*, 24–43. https://doi.org/10.1016/j.lithos.2018.01.012

Ferrando, C., Lynn, K. J., Basch, V., Ildefonse, B., & Godard, M. (2020). Retrieving timescales of oceanic crustal evolution at Oceanic Core Complexes: Insights from diffusion modelling of geochemical profiles in olivine. *Lithos*, *376–377*, 105727. https://doi.org/10.1016/j.lithos.2020.105727

France, L., Ildefonse, B., & Koepke, J. (2009). Interactions between magma and hydrothermal system in Oman ophiolite and in IODP Hole 1256D: Fossilization of a dynamic melt lens at fast spreading ridges. *Geochemistry, Geophysics, Geosystems*, *10*, Q10O19. https://doi.org/10.1029/2009GC002652

Gao, Y., Hoefs, J., Hellebrand, E., von der Handt, A., & Snow, J. (2007). Trace element zoning in pyroxenes from ODP Hole 735B gabbros: Diffusive exchange or synkinematic crystal fractionation? *Contributions to Mineralogy and Petrology*, *153*, 429–442. https://doi.org/10.1007/s00410-006-0158-4

Ghiorso, M. S., & Sack, R. O. (1995). Chemical mass transfer in magmatic processes. IV. A revised and internally consistent thermodynamic model for the interpolation and extrapolation of liquid-solid equilibria in magmatic systems at elevated temperatures and pressures. *Contributions to Mineralogy and Petrology*, *119*, 197–212. https://doi.org/10.1007/BF00307281

Gillis, K., Snow, J., & Klaus, A., & the Expedition 345 Scientists. (2014). Proceedings of the Integrated Ocean Drilling Program (Vol. *345*, Initial Reports). College Station, TX: Integrated Ocean Drill Program Manage Int. https://doi.org/10.2204/iodp.proc.345.101.2014

Godard, M., Awaji, S., Hansen, H., Hellebrand, E., Brunelli, D., Johnson, K., et al. (2009). Geochemistry of a long in-situ section of intrusive slow-spread oceanic lithosphere: Results from IODP Site U1309 (Atlantis Massif, 30°N Mid-Atlantic-Ridge). *Earth and Planetary Science Letters*, *279*, 110–122. https://doi.org/10.1016/j.epsl.2008.12.034

Gracia, E., Bideau, D., Hekinian, R., & Lagabrielle, Y. (1999). Detailed geological mapping of two contrasting second-order segments of the Mid-Atlantic Ridge between Oceanographer and Hayes fracture zones (33°30'N-35°N). *Journal of Geophysical Research*, *104*, 22903–22921. https://doi.org/10.1029/1999JB900161

Grimes, C. B., John, B. E., Cheadle, M. J., & Wooden, J. L. (2008). Protracted construction of gabbroic crust at a slow spreading ridge: Constraints from 206Pb/238U zircon ages from Atlantis Massif and IODP Hole U1309D (30°N, MAR). *Geochemistry, Geophysics, Geosystems*, *9*. https://doi.org/10.1029/2008GC002063

Grove, T. L., Kinzler, R. J., & Bryan, W. B. (1992). Fractionation of mid-ocean ridge basalt (MORB). *Geophysical Monograph Series*, *71*, 281–310. https://doi.org/10.1029/GM071p0281

Hammer, J. E., & Rutherford, M. J. (2002). An experimental study of the kinetics of decompression-induced crystallization in silicic melt. *Journal of Geophysical Research*, *107*, B1. https://doi.org/10.1029/2001JB000281

Hersum, T., Hilpert, M., & Marsh, B. (2005). Permeability and melt flow in simulated and natural partially molten basaltic magmas. *Earth and Planetary Science Letters*, *237*, 798–814. https://doi.org/10.1016/j.epsl.2005.07.008

Holness, M. B., Anderson, A. T., Martin, V. M., Maclennan, J., Passmore, E., & Schwindinger, K. (2007). Textures in partially solidified crystalline nodules: A window into the pore structure of slowly cooled mafic intrusions. *Journal of Petrology*, *48*, 1243–1264. https://doi.org/10.1093/petrology/egm016

Husen, A., Almeev, R. R., & Holtz, F. (2016). The effect of H₂O and pressure on multiple saturation and liquid lines of descent in basalt from the Shatsky Rise. *Journal of Petrology*, *57*, 309–344. https://doi.org/10.1093/petrology/egw008

Jackson, M. D., Blundy, J., & Sparks, R. S. J. (2018). Chemical differentiation, cold storage and remobilization of magma in the Earth's crust. *Nature*, *564*, 405–409. https://doi.org/10.1038/s41586-018-0746-2

Jian, H., Singh, S. C., Chen, Y. J., & Li, J. (2017). Evidence of an axial magma chamber beneath the ultraslow-spreading Southwest Indian Ridge. *Geology*, *45*, 143–14644. https://doi.org/10.1130/G38356.1

John, B. E., Foster, D. A., Murphy, J. M., Cheadle, M. J., Baines, A. G., Fanning, C. M., & Copeland, P. (2004). Determining the cooling history of in situ lower oceanic crust-Atlantis Bank, SW Indian Ridge. *Earth and Planetary Science Letters*, *222*, 145–160. https://doi.org/10.1016/j.epsl.2004.02.014

Kelemen, P. B. (1990). Reaction between ultramafic rock and fractionating basaltic magma I. phase relations, the origin of calc-alkaline magma series, and the formation of discordant dunite. *Journal of Petrology*, *31*, 51–98. https://doi.org/10.1093/petrology/31.1.51

Kelley, D. S., & Fruh-Green, G. L. (2001). Volatile lines of descent in submarine plutonic environments: Insights from stable isotope and fluid inclusion analyses. *Geochimica et Cosmochimica Acta*, *65*, 3325–3346. https://doi.org/10.1016/S0016-7037(01)00667-6

Kirkpatrick, R. J., Robinson, G. R., & Hays, J. F. (1976). Kinetics of crystal growth from silicate melts: Anorthite and diopside. *Journal of Geophysical Research*, *81*(32), 5715–5720. https://doi.org/10.1029/JB081i032p05715

Koepke, J., Botcharnikov, R. E., & Natland, J. H. (2018). Crystallization of late-stage MORB under varying water activities and redox conditions: Implications for the formation of highly evolved lavas and oxide gabbro in the ocean crust. *Lithos*, *323*, 58–77. https://doi.org/10.1016/j.lithos.2018.10.001

Koepke, J., France, L., Müller, T., Faure, F., Goetze, N., Dziony, W., & Ildefonse, B. (2011). Gabbros from IODP Site 1256, equatorial Pacific: Insight into axial magma chamber processes at fast spreading ocean ridges. *Geochimica et Cosmochimica Acta*, *12*, Q09014. https://doi.org/10.1029/2011GC003655

Korenaga, J., & Kelemen, P. B. (1997). Origin of gabbro sills in the Moho transition zone of the Oman ophiolite: Implications for magma transport in the oceanic lower crust. *Journal of Geophysical Research*, *102*, 27729–27749. https://doi.org/10.1029/97JB02604

Korenaga, J., & Kelemen, P. B. (1998). Melt migration through the oceanic lower crust: A constraint from melt percolation modeling with finite solid diffusion. *Earth and Planetary Science Letters*, *156*, 1–11. https://doi.org/10.1016/S0012-821X(98)00004-1

Kvassnes, A., & Grove, T. (2008). How partial melts of mafic lower crust affect ascending magmas at oceanic ridges. *Contributions to Mineralogy and Petrology*, *156*, 49–71. https://doi.org/10.1007/s00410-007-0273-x

Langmuir, C. H. (1989). Geochemical consequences of in situ crystallization. *Nature*, *340*, 199–205. https://doi.org/10.1038/340199a0

Le Roux, V., Dasgupta, R., & Lee, C. T. A. (2011). Mineralogical heterogeneities in the Earth's mantle: Constraints from Mn, Co, Ni and Zn partitioning during partial melting. *Earth and Planetary Science Letters*, *307*, 395–408. https://doi.org/10.1016/j.epsl.2011.05.014

Leuthold, J., Blundy, J. D., Holness, M. B., & Sides, R. (2014). Successive episodes of reactive liquid flow through a layered intrusion (Unit 9, Rum Eastern Layered Intrusion, Scotland). *Contributions to Mineralogy and Petrology*, *168*, 1021. https://doi.org/10.1007/s00410-014-1021-7

Lissenberg, C. J., & Dick, H. J. B. (2008). Melt-rock reaction in the lower oceanic crust and its implications for the genesis of mid-ocean ridge basalt. *Earth and Planetary Science Letters*, *271*, 311–325. https://doi.org/10.1016/j.epsl.2008.04.023

Lissenberg, C. J., & MacLeod, C. J. (2016). A reactive porous flow control on mid-ocean ridge magmatic evolution. *Journal of Petrology*, *57*, 2195–2220. https://doi.org/10.1093/petrology/egw074

Lissenberg, C. J., MacLeod, C. J., & Bennett, E. N. (2019). Consequences of a crystal mush-dominated magma plumbing system: A mid-ocean ridge perspective. *Philosophical Transactions of the Royal Society A*, *377*, 2139. https://doi.org/10.1098/rsta.2018.0014

Lissenberg, C. J., MacLeod, C. J., Howard, K. A., & Godard, M. (2013). Pervasive reactive melt migration through fast-spreading lower oceanic crust (Hess Deep, equatorial Pacific Ocean). *Earth and Planetary Science Letters*, *361*, 436–447. https://doi.org/10.1016/j.epsl.2012.11.012

Lofgren, G. E. (1980). Experimental studies on the dynamic crystallization of silicate melts. In R. B. Hargraves (Ed.), *Physics of magnetic processes* (pp. 487–551). Princeton, NJ: Princeton University Press.

MacLeod, C. J., Dick, H. J. B., Blum, P., Abe, N., Blackman, D. K., Bowles, J. A., et al. (2017). Proceedings of the Integrated Ocean Discovery Program (Vol. *360*). https://doi.org/10.14379/iodp.proc.360.103.2017

MacLeod, C. J., Searle, R. C., Murton, B. J., Casey, J. F., Mallows, C., Unsworth, S. C., et al. (2009). Life cycle of oceanic core complexes. *Earth and Planetary Science Letters*, *287*, 333–344. https://doi.org/10.1016/j.epsl.2009.08.016

Martel, C. (2012). Eruption Dynamics Inferred from Microlite Crystallization Experiments: Application to Plinian and dome-forming eruptions of Mt Pelée (Martinique, Lesser Antilles). *Journal of Petrology*, *53*(4), 699–725. https://doi.org/10.1093/petrology/egr076

Meyer, P. S., Dick, H. J. B., & Thompson, G. (1989). Cumulate gabbros from the Southwest Indian Ridge, 54° S-7°16′ E: Implications for magmatic processes at a slow spreading ridge. *Contributions to Mineralogy and Petrology*, *103*, 44–63. https://doi.org/10.1007/BF00371364

Mollo, S., & Hammer, J. E. (2017). Dynamic crystallization in magmas. In W. Heinrich, & R. Abart (Eds.), *Mineral reaction kinetics: Microstructures, textures, chemical and isotopic signatures* (Vol. *16*, pp. 373–418). EMU Notes in Mineralogy. https://doi.org/10.1180/EMU-notes.16.12

Mourey, A. J., & Shea, T. (2019). Forming olivine phenocrysts in basalt: A 3D characterization of growth rates in laboratory experiments. *Frontiers in Earth Science*, *7*, 300. https://doi.org/10.3389/feart.2019.00300

Natland, J. H., & Dick, H. J. B. (2001). Formation of the lower ocean crust and the crystallization of gabbroic cumulates at a very slowly spreading ridge. *Journal of Volcanology and Geothermal Research*, *110*, 191–233. https://doi.org/10.1016/S0377-0273(01)00211-6

Nielsen, T. F. D., Andersen, J. C. Ø., Holness, M. B., Keiding, J. K., Rudashevsky, N. S., Rudashevsky, V. N., et al. (2015). The Skaergaard PGE and gold deposit: The result of in situ fractionation, sulphide saturation, and magma chamber-scale precious metal redistribution by immiscible Fe-rich melt. *Journal of Petrology*, *56*(8), 1643–1676. https://doi.org/10.1093/petrology/egv049

O'Driscoll, B. (2005). Textural equilibrium in magmatic layers of the syn-tectonic Lough Fee ultramafic intrusion, NW Connemara: Implications for adcumulus mineral growth. *Irish Journal of Earth Sciences*, *23*, 39–45.

O'Driscoll, B., Donaldson, C. H., Troll, V. R., Jerram, D. A., & Emeleus, C. H. (2007). An origin for harrisitic and granular olivine in the rum layered suite, NW Scotland: A crystal size distribution study. *Journal of Petrology*, *48*, 253–270. https://doi.org/10.1093/petrology/egl059

O'Hara, M. J., & Fry, N. (1996). The highly compatible trace element paradox-fractional crystallization revisited. *Journal of Petrology*, *37*, 859–890. https://doi.org/10.1093/petrology/37.4.859

O'Neill, H. S., & Jenner, F. E. (2012). The global pattern of trace element distributions in ocean floor basalts. *Nature*, *491*, 698–705. https://doi.org/10.1038/nature11678

Pearce, N. J. G., Perkins, W. T., Westgate, J. A., Gorton, M. P., Jackson, S. E., Neal, C. R., & Chenery, S. P. (1997). A compilation of new and published major and trace element data for NIST SRM 610 and NIST SRM 612 glass reference materials. *Geostandards Newsletter: The Journal of Geostandards and Geoanalysis*, *21*(1), 115–144. https://doi.org/10.1111/j.1751-908X.1997.tb00538.x

Rampone, E., Borghini, G., Godard, M., Ildefonse, B., Crispini, L., & Fumagalli, P. (2016). Melt/rock reaction at oceanic peridotite/gabbro transition as revealed by trace element chemistry of olivine. *Geochimica et Cosmochimica Acta*, *190*, 309–331. https://doi.org/10.1016/j.gca.2016.06.029

Roeder, P. L., & Emslie, R. F. (1970). Olivine-liquid equilibrium. *Contributions to Mineralogy and Petrology*, *29*, 277–302. https://doi.org/10.1007/BF00371276

Ross, D. K., & Elthon, D. (1997). Cumulus and postcumulus crystallization in the oceanic crust: Major- and trace-element geochemistry of Leg 153 gabbroic rocks. *Proceedings of the Ocean Drilling Program, Scientific Results*, *153*, 333–353. https://doi.org/10.2973/odp.proc.sr.153.023.1997

Sanfilippo, A., Dick, H. J. B., & Ohara, Y. (2013). Melt-rock reaction in the mantle: Mantle troctolites from the Parece Vela ancient back-arc spreading center. *Journal of Petrology*, *54*, 861–885. https://doi.org/10.1093/petrology/egs089

Sanfilippo, A., MacLeod, C. J., Tribuzio, R., Lissenberg, C. J., & Zanetti, A. (2020). Early-stage melt-rock reaction in a cooling crystal mush beneath a slow-spreading mid-ocean ridge (IODP Hole U1473A, Atlantis Bank, Southwest Indian Ridge). *Frontiers in Earth Science, 8*, 579138. https://doi.org/10.3389/feart.2020.579138

Sanfilippo, A., Tribuzio, R., & Tiepolo, M. (2014). Mantle-crust interactions in the oceanic lithosphere: Constraints from minor and trace elements in olivine. *Geochimica et Cosmochimica Acta*, *141*, 423–439. https://doi.org/10.1016/j.gca.2014.06.012

Sanfilippo, A., Tribuzio, R., Tiepolo, M., & Berno, D. (2015). Reactive flow as dominant evolution process in the lowermost oceanic crust: Evidence from olivine of the Pineto ophiolite (Corsica). *Contributions to Mineralogy and Petrology*, *170*, 38. https://doi.org/10.1007/s00410-015-1194-8

Saper, L., & Liang, Y. (2014). Formation of plagioclase-bearing peridotite and plagioclase-bearing wehrlite and gabbro suite through reactive crystallization: An experimental study. *Contributions to Mineralogy and Petrology*, *167*, 1–16. https://doi.org/10.1007/s00410-014-0985-7

Shea, T., Hammer, J. E., Hellebrand, E., Mourey, A. J., Costa, F., First, E. C., et al. (2019). Phosphorus and aluminum zoning in olivine: Contrasting behavior of two nominally incompatible trace elements. *Contributions to Mineralogy and Petrology*, *174*, 85. https://doi.org/10.1007/s00410-019-1618-y

Singh, S. C., Crawford, W. C., Carton, H., Seher, T., Combier, V., Cannat, M., et al. (2006). Discovery of a magma chamber and faults beneath a Mid-Atlantic Ridge hydrothermal field. *Nature*, *442*, 1029–1032. https://doi.org/10.1038/nature05105

Sinha, M. C., Navien, D. A., MacGregor, L. M., Constable, S., Peirce, C., White, A., et al. (1997). Evidence for accumulated melt beneath the slow-spreading Mid-Atlantic Ridge. *Philosophical Transactions of the Royal Society of London*, *355*, 1723. https://doi.org/10.1098/rsta.1997.0008

Sinton, J. M., & Detrick, R. S. (1992). Mid-ocean ridge magma chambers. *Journal of Geophysical Research*, *97*, 197–216. https://doi.org/10.1029/91JB02508

Solano, J. M. S., Jackson, M. D., Sparks, R. S. J., & Blundy, J. (2014). Evolution of major and trace element composition during melt migration through crystalline mush: Implications for chemical differentiation in the crust. *American Journal of Science*, *314*, 895–939. https://doi.org/10.2475/05.2014.01

Sun, C., Graff, M., & Liang, Y. (2017). Trace element partitioning between plagioclase and silicate melt: The importance of temperature and plagioclase composition, with implications for terrestrial and lunar magmatism. *Geochimica et Cosmochimica Acta*, *206*, 273–295. https://doi.org/10.1016/j.gca.2017.03.003

Sun, C., & Liang, Y. (2012). Distribution of REE between clinopyroxene and basaltic melt along a mantle adiabat: Effects of major element composition, water, and temperature. *Contributions to Mineralogy and Petrology*, *163*, 807–823. https://doi.org/10.1007/s00410-011-0700-x

Sun, C., & Liang, Y. (2013). The importance of crystal chemistry on REE partitioning between mantle minerals (garnet, clinopyroxene, orthopyroxene, and olivine) and basaltic melts. *Chemical Geology*, *358*, 23–36. https://doi.org/10.1016/j.chemgeo.2013.08.045

Sun, C., & Liang, Y. (2014). An assessment of subsolidus re-equilibration on REE distribution among mantle minerals olivine, orthopyroxene, clinopyroxene, and garnet in peridotites. *Chemical Geology*, *372*, 80–91. https://doi.org/10.1016/j.chemgeo.2014.02.014

Sun, S.-s., & McDonough, W. F. (1989). Chemical and isotopic systematics of oceanic basalts: Implications for mantle composition and processes. *Geological Society, London, Special Publications*, *42*, 313–345. https://doi.org/10.1144/GSL.SP.1989.042.01.19

Teagle, D. A. H., Alt, J. C., Umino, S., Miyashita, S., Banerjee, N. R., & Wilson, D. S., & the Expedition 309/312 Scientists. (2006). *Proceedings IODP, 309/312*. Washington, DC: Integrated Ocean Drilling Program Management International, Inc. https://doi.org/10.2204/iodp.proc.309312.2006

Tribuzio, R., Tiepolo, M., & Vannucci, R. (2000). Evolution of gabbroic rocks of the Northern Apennine ophiolites (Italy): Comparison with the lower oceanic crust from modern slow-spreading ridges. In Y. Dilek, E. M. Moores, D. Elthon, & A. Nicolas (Eds.), Ophiolites and oceanic crust: New insights from field studies and the Ocean Drilling Program (Vol. 349, pp. 129–138): Geological Society of America Special Papers. https://doi.org/10.1130/0-8137-2349-3.129

Tucholke, B. E., Lin, J., Kleinrock, M. C., Tivey, M. A., Reed, T. B., Goff, J., & Jaroslow, G. E. (1997). Segmentation and crustal structure of the western Mid-Atlantic Ridge flank, 25°25'-27°10' N and 0-29 m.y. *Journal of Geophysical Research*, *102*, 10203–10223. https://doi.org/10.1029/96JB03896

Van Achterberg, E., Ryan, C. G., Jackson, S. E., & Griffin, W. (2001). Data reduction software for LA-ICP-MS. In P. Sylvester (Ed.), *Laser ablation ICP-MS in the Earth Science* (pp. 239–243). Mineralogical Association of Canada.

Van den Bleeken, G., Müntener, O., & Ulmer, P. (2011). Melt variability in percolated peridotite: An experimental study applied to reactive migration of tholeiitic basalt in the upper mantle. *Contributions to Mineralogy and Petrology*, *161*, 921–945. https://doi.org/10.1007/s00410-010-0572-5

Vanko, D. A., & Stakes, D. S. (1991). Fluids in oceanic layer 3: Evidence from veined rocks, Hole 735B, southwest Indian Ridge. In R. P. Von Herzen, & P. T. Robinson (Eds.), *Proceedings of the Ocean Drill Program, scientific results* (Vol. *118*, pp. 181–215). College Station, TX: Ocean Drill Program. https://doi.org/10.2973/odp.proc.sr.118.121.1991

Van Orman, J. A., Cherniak, D. J., & Kita, N. T. (2014). Magnesium diffusion in plagioclase: Dependence on composition, and implications for thermal resetting of the ^{26}Al-^{26}Mg early solar system chronometer. *Earth and Planetary Science Letters*, *385*, 79–88. https://doi.org/10.1016/j.epsl.2013.10.026

Villiger, S., Ulmer, P., & Müntener, O. (2007). Equilibrium and fractional crystallization experiments at 0.7 GPa: The effect of pressure on phase relations and liquid compositions of tholeiitic magmas. *Journal of Petrology*, *48*, 159–184. https://doi.org/10.1093/petrology/egl058

Welsch, B., Faure, F., Famin, V., Baronnet, A., & Bachèlery, P. (2013). Dendritic crystallization: A single process for all the textures of olivine in basalts? *Journal of Petrology*, *54*, 539–574. https://doi.org/10.1093/petrology/egs077

Yang, A. Y., Wang, C., Liang, Y., & Lissenberg, C. J. (2019). Reaction between mid-ocean ridge basalt and lower oceanic crust: An experimental study. *Geochemistry, Geophysics, Geosystems*, *20*, 4390–4407. https://doi.org/10.1029/2019GC008368

Zhang, W. Q., Liu, C. Z., & Dick, H. J. B. (2020). Evidence for multi-stage melt transport in the lower ocean crust: Atlantis Bank Gabbroic Massif (IODP Hole U1473A, SW Indian Ridge). *Journal of Petrology*, egaa082. https://doi.org/10.1093/petrology/egaa082